This is a preprint, the final version is subject to change, of the American Mineralogist (MSA)
Cite as Authors (Year) Title. American Mineralogist, in press.
DOI: https://doi.org/10.2138/am-2020-7303

A multi-method characterization of natural terrestrial birnessites

Florence T. Ling[1,2,*], Jeffrey E. Post[3], Peter J. Heaney[1], Cara M. Santelli[4], Eugene S. Ilton[5], William D. Burgos[6], Arthur W. Rose[1]

[1]Department of Geosciences, Penn State University, University Park, PA 16802, USA,
[2]Department of Biology, Environmental Science Program, La Salle University, Philadelphia, PA 19141, USA
*ling@lasalle.edu
[3]Department of Mineral Sciences, NHB 119, Smithsonian Institute, Washington, DC 20013-7012, USA
[4]Department of Earth and Environmental Sciences, University of Minnesota, Minneapolis, MN 55455
[5]Pacific Northwest Laboratory, 902 Battelle Blvd, Richland, WAV 99352, USA
[6]Department of Civil and Environmental Engineering, Penn State University, University Park, PA 16802, USA

This is a preprint, the final version is subject to change, of the American Mineralogist (MSA)
Cite as Authors (Year) Title. American Mineralogist, in press.
DOI: https://doi.org/10.2138/am-2020-7303

ABSTRACT

With a focus on a large set of natural birnessites collected from terrestrial, freshwater systems, we applied and compared the capabilities of X-ray diffraction (XRD), extended X-ray absorption fine structure (EXAFS), Fourier-transform infrared spectroscopy (FTIR), and X-ray photoelectron spectroscopy (XPS) to characterize crystal structure and chemistry. Using XRD, we successfully identified 3 of the 11 natural birnessite samples as hexagonal ranciéite-like phases, but the remaining samples yielded less interpretable "3-line" diffraction patterns with broad, asymmetrical peaks at d-spacings of ~7.2 Å, ~2.4 Å, and ~1.4 Å. EXAFS analysis suggested that many of these samples had characteristics of both triclinic and hexagonal birnessite. However, application of EXAFS to the ranciéite-like phases yielded unreasonably high concentrations of triclinic birnessite as an intergrowth, calling into question the use of synthetic hexagonal H-birnessite as an appropriate standard in the linear combination fitting of EXAFS data for natural birnessites. FTIR spectroscopy of the "3-line" birnessite samples successfully distinguished triclinic and hexagonal constituents, and analyses of peak positions suggested that natural birnessites occur as a full spectrum of triclinic and hexagonal intergrowths. XPS analysis of these samples revealed that higher Mn^{3+} concentrations relative to Mn^{2+} and Mn^{4+} are correlated to increased proportions of triclinic birnessite.

KEYWORDS: manganese oxide, birnessite, FTIR, EXAFS, XPS, XRD

INTRODUCTION

Manganese oxides occur in a wide variety of surficial environments, for example as fine-grained sediments in soils, as nodules in lakes and oceans, and as coatings on rock surfaces (Post 1999). Their fine grain sizes and high surface areas result in their high reactivity, and Mn oxides consequently play a vital role in heavy metal cycling and redox reactions occurring in the environment (Paterson et al. 1986; Lopano et al. 2007, 2009, 2011; Fleeger et al. 2013). For instance, Mn oxides can sorb Zn, Sn, and Ni (Chao and Theobald 1976; Usui and Mita 1994), and they can oxidize Se^{4+} to Se^{6+}, Cr^{3+} to Cr^{6+}, and Co^{2+} to Co^{3+}, just a few of the redox reactions in which Mn oxides are involved (Bartlett and James 1979; Murray and Dillard 1979; Oscarson et al. 1981; Scott and Morgan 1996; Kay et al. 2001; Fandeur et al. 2009; Lafferty et al. 2011; Peacock and Moon 2012; Kazakis et al. 2015; Kong et al. 2019). Due to their high reactivity with organic carbon, they also play a role in carbon cycling, making Mn oxides an important mineral for modeling the role of mineral-carbon reactions in climate change (Remucal and Ginder-Vogel 2014; Johnson et al. 2015; Allard et al. 2017; Stuckey et al., 2018).

The layered Mn oxide minerals in the birnessite family are widely studied for their natural occurrence in a range of terrestrial settings and for their chemical reactivity (Potter and Rossman 1979; Post 1999; McKeown and Post 2001; Manceau et al. 2002, 2007; Weaver and Hochella 2003). Birnessites exist as two symmetries, triclinic and hexagonal (Fig. 1). According to Post and Veblen (1990) and Post et al. (2002), synthetic triclinic Na-birnessite ($Na_{0.58}(Mn^{4+}_{1.42}Mn^{3+}_{0.58})O_4 \bullet 1.5H_2O$) consists of layered Mn octahedral sheets with ~71% Mn^{4+} and ~29% Mn^{3+}, along with hydrated Na^+ cations in the interlayer sites. In contrast, Silvester et al. (1997) describe synthetic hexagonal H-birnessite ($H_{0.33}Mn^{3+}_{0.111}Mn^{2+}_{0.055}(Mn^{4+}_{0.722}Mn^{3+}_{0.111}\square_{0.167})O_2$) as having Mn octahedral sheets consisting of ~72% Mn^{4+} cations, ~11% Mn^{3+}

cations, and ~17% vacancies, along with Mn^{2+}, Mn^{3+}, and H^{+} cations that occupy the interlayer near the octahedral vacancy sites. As the Mn oxidation states and the vacancy concentrations are different for triclinic and hexagonal birnessite, they can behave differently in similar geochemical environments. The vacancies in hexagonal birnessite, for example, act as sites for the sorption of Pb and Zn (Toner et al. 2006; Kwon et al. 2010). In contrast, the absence of octahedral vacancies in triclinic birnessite diminishes the capacity for transition metal uptake (Wang et al. 2012). Moreover, Mn^{3+}, which exists in higher concentrations in triclinic birnessite, plays a role in the oxidation of Cr^{3+} to Cr^{6+} and Co^{2+} to Co^{3+} (Manceau et al. 1992; Weaver and Hochella 2003; Simanova and Peña 2015; Kong et al. 2019). Identifying the structural characteristics of a natural birnessite sample can help predict which chemical processes will dominate.

The characterization of natural birnessites is challenged by their small particle size and poor crystallinity. X-ray diffraction (XRD), a standard method for phase identification, often falls short of properly identifying natural Mn oxides due to the absence of long-range order (Post 1999). Birnessite, specifically, is distinguished by its ~7 Å d-spacing. In many natural samples, the birnessite may initially be identified as buserite, the hydrated relative of birnessite that has a distinct ~10 Å spacing. Upon heating buserite to 110°C, the 10 Å spacing collapses as interlayer water is lost, yielding the ~7 Å spacing of birnessite. This collapse distinguishes birnessite from todorokite, which has a ~10 Å peak that does not collapse upon heating at 110°C (Usui & Mita 1994). This method of identifying natural birnessites is widely utilized (Post 1999; Bilinski et al. 2002; Zhao et al. 2012; Frierdich et al. 2011), but when diagnostic X-ray diffraction peaks are not evident, XRD may not be able to reveal whether a birnessite is triclinic or hexagonal. The situation is complicated further by the conventional use of Cu rather than, for example, Mo X-

ray radiation, since the absorption edge for Cu is close to that of Mn and absorption and fluorescence greatly degrade the signal-to-noise ratio (SI Fig. 1).

Instead, synchrotron X-ray absorption spectroscopy (XAS) has been employed extensively for the structural characterization of Mn oxides by focusing on the bonding environment surrounding Mn atoms. XAS is particularly useful for samples containing minor amounts of Mn or for identifying the coordination of other elements on or within Mn oxides, and has also been used to identify the phase distributions in poorly crystalline natural Mn oxides and those precipitated by bacteria and fungi in laboratory cultures. Unlike X-ray diffraction analysis of "3-line" birnessite, XAS sometimes can offer insights into the relative concentrations of triclinic and hexagonal birnessite through linear combination fitting (LCF) and/or modeling of the extended absorption fine structure (EXAFS) or X-ray absorption near edge structure (XANES) regions (Jürgensen et al. 2004; Webb et al. 2005a, 2005b; Villalobos et al. 2006; Bargar et al. 2009; Saratovsky et al. 2009; Learman et al. 2011; Santelli et al. 2011; Hinkle et al. 2016).

Most studies of natural birnessites in freshwater environments presume that they form through a mix of biotic and abiotic processes. For phases that form biotically, it is hypothesized that biogenic birnessites precipitate at least initially as δ-MnO_2, a form of hexagonal birnessite. This interpretation originates from laboratory experiments in which hexagonal birnessite has consistently been observed as the first phase produced under most chemical conditions examined (Villalobos et al. 2003, 2006; Bargar et al. 2005; Saratovsky et al. 2006; Learman et al. 2011; Santelli et al. 2011; Hansel et al. 2012). Whether or not these laboratory phases are representative of natural minerals needs greater investigation as some recent studies have shown that certain synthetic media components may impact the Mn oxide structures. Specifically,

Good's buffers, used regularly in biological growth experiments because they are non-toxic and thought to be biochemically inert, can force the formation of hexagonal birnessite under abiotic conditions (Ling et al. 2015; Simanova et al. 2015), potentially skewing results of bioprecipitation experiments with bacteria and fungi. Although "pseudo-orthogonal" birnessite and the tunnel-structured Mn oxide todorokite have been reported as secondary crystallization phases (Webb et al. 2005b; Feng et al. 2010), and Tan et al. (2010) observed that both triclinic and hexagonal can co-exist in natural environments, most experimental work uses a form of synthetic hexagonal birnessite for investigations into the reactivity of Mn oxides in natural environments. More work is required to characterize natural birnessites to enhance our knowledge of which birnessite varieties are most prevalent and how other phases contribute to birnessite-mediated reactions and, ultimately, impact the environment.

By characterizing eleven birnessite samples from a variety of nonmarine environments using a suite of analytical approaches, here we explore the variety of natural birnessites that prevail in terrestrial, freshwater systems. We interrogated the samples with scanning electron microscopy coupled with energy dispersive X-ray spectroscopy (SEM/EDS), electron microprobe analysis (EPMA), X-ray diffraction, X-ray absorption spectroscopy, and X-ray photoelectron spectroscopy (XPS) to survey the chemical compositions and Mn oxidation state ratios of naturally occurring birnessites. Following the demonstration by Ling et al. (2016) that Fourier-transform infrared spectroscopy (FTIR) can differentiate between synthetic triclinic and hexagonal birnessites, we also applied FTIR to natural birnessites, and we evaluated the relative accuracy and ease of these techniques to gauge their suitability for birnessite characterization.

METHODS

Samples

Synthesis of standard triclinic birnessite. Triclinic Na-birnessite was synthesized according to the procedure described in Golden et al. (1986). A 200 ml solution of 0.5 M $MnCl_2$ (Mallinckrodt Baker) was mixed with 250 ml of 5.5 M NaOH (J.T. Baker). The mixture was oxygenated through a glass frit for ~5 hrs at a rate of 1.5 L/min. The precipitate was divided evenly and centrifuged in 14 centrifuge tubes. The solution was decanted and replaced with pH 6.49 deionized (DI) water to rinse. The rinse cycle was repeated five times. Na-birnessite was stored in ~350 ml DI water until experimental use. For experiments, aliquots of Na-birnessite were filtered with a 0.05 μm Nuclepore Track-Etched polycarbonate membrane filter (Whatman), rinsed three times with 100 ml DI water, and left to air-dry at room temperature. X-ray diffraction with a Rigaku D/MAX-RAPID microdiffractometer using a Mo tube source (λ = 0.71069 Å) confirmed the synthesis of triclinic birnessite.

Synthesis of standard hexagonal birnessite. Our hexagonal birnessite standard was synthesized by reacting ~100 mg of dried triclinic Na-birnessite in 100 ml of 0.01 M HCl for 24 hrs. The H-birnessite then was filtered with a 0.05 μm Nuclepore Track-Etched polycarbonate membrane filter (Whatman), rinsed three times with 100 ml DI water, and left to air-dry. X-ray diffraction confirmed the synthesis of hexagonal birnessite.

Synthetic fungal sample. The fungal species *Stagnospora sp*. SRC11sM3a was obtained from a passive acid mine drainage remediation system in Central Pennsylvania that effectively removed high concentrations of Mn through precipitation of Mn oxides as described in Santelli et al. (2010). The culture was inoculated in a 20 mM pH 7 HEPES-buffered AY medium that consisted of 0.25 g L^{-1} sodium acetate, 0.15 g L^{-1} yeast extract, 1 mL L^{-1} trace elements stock (10 mg L^{-1} $CuSO_4 \cdot 5H_2O$, 44 mg L^{-1} $ZnSO_4 \cdot 7H_2O$, 20 mg L^{-1} $CoCl_2 \cdot 6H_2O$, 13 mg L^{-1}

158 $Na_2MoO_4 \cdot 2H_2O$), and supplemented with 150 μM $MnCl_2$ and 0.1 mM $CaCl_2$. Mn was held
159 constant during growth for ~20 days, but not supplemented after. The selected conditions were
160 chosen to simulate the average geochemical conditions measured in the treatment systems during
161 sampling. The culture was grown in 50 mL of liquid AY medium without agitation to resemble
162 a submerged environment, and incubated in the dark at room temperature for ~20 – 24 days and
163 stored in dark conditions to prevent photoreduction of Mn oxides.

164 **Natural samples.** We collected four birnessite-containing samples from passive coal
165 mine drainage treatment sites near the central Pennsylvania towns of De Sale (near Eau Claire,
166 Butler Co.) (labeled DS1-M3f and DS2-M3f) and Central City in Somerset Co. (labeled PBS-
167 M3f-1 and PBS-M3f-2) (Table 1). The treatment systems consist of rectangular beds filled with
168 crushed limestone to ~1 m in depth. The coal mine drainage horizontally flowed through the
169 limestone beds on which Mn oxide sediments precipitated. Further descriptions of sampling
170 methods and localities for the De Sale and the Central City specimens are described in Tan et al.
171 (2010) and Luan et al. (2012). Likewise, we collected another birnessite sample (labeled
172 Glasgow) from a similar passive coal mine drainage treatment site in Glasgow near Tyrone, Blair
173 Co., PA. The powder was recovered from a Metal Removal Unit (MRU) built by EcoIslands
174 LLC. The MRUs consisted of ~6 ft x 4 ft plywood boxes, with each box divided into 3 sections
175 containing coconut coir fiber (SI Fig. 2). The influent water to the MRUs was analyzed monthly,
176 with Mn concentrations from 26.4 mg/L to 39.8 mg/L. The MRUs were partially drained to
177 allow settling of sediment particles prior to sample collection. Mn oxide coatings were scraped
178 off the coconut coir for analysis. We recognize that these samples are produced from engineered
179 systems, but we will refer to them as natural samples for this work with the understanding that
180 the conditions are likely similar to those of natural freshwater systems that form birnessite.

Another birnessite-containing sample (labeled Spring Branch) originated as a Mn oxide coating on limestone cobbles from a stream in Spring Branch, TN, and this site was deemed a natural environmental analog to the Pennsylvania acid mine remediation sites. In contrast, we also studied a sample from Lake Vermilion in northeastern MN (kindly provided by Michael G. Sommers). The sampling method and site description are detailed in Sommers et al. (2002), with this particular sample described as a "reef-type stromatolite" based on its reef-like shape and resemblance to biotically precipitated specimens.

The remaining samples were provided by the Smithsonian's Mineral Reference Collection in the Department of Mineral Sciences, National Museum of Natural History. Mn oxides from Paxton Cave, VA (Smithsonian Institution NMNH #160078) were identified as ranciéite in previous studies (Richmond et al. 1969). Ranciéite is a Ca-rich member of the birnessite family with hexagonal symmetry (Post et al. 2008). Ranciéite from Spain originated in an abandoned open pit Fe/Mn mine near Trevelez, Las Alpujaras, Granada, Spain. Finally, the one ranciéite sample that might have formed at slightly elevated temperatures (Smithsonian Institution NMNH #128319) was collected from a hydrothermal vein in the French Pyrenees.

X-ray diffraction (XRD)

All samples were lightly ground in an agate mortar under acetone to disaggregate clumps. For XRD analysis, ~2 mg of sample were mounted on glass fibers and data were collected using a Rigaku D/MAX-RAPID microdiffractometer with an imaging plate detector (Smithsonian Institution, Mineral Sciences Department) and a Mo tube source (λ = 0.71069 Å). Samples were rotated 360° around the *phi* axis at 1° s^{-1} during data collection with a 10 min exposure time. XRD data were analyzed using JADE 2010 (Materials Data, Inc.).

204

205 **Scanning electron microscopy/energy dispersive spectroscopy (SEM/EDS)**

206 A FEI Nova NanoSEM 600 (Department of Mineral Sciences, Smithsonian Institution)
207 operating at an accelerating voltage of 15 keV and a beam current of 1 to 2 nA, and equipped
208 with a ThermoFisher energy dispersive X-ray detector (EDS), was used for elemental analyses of
209 the birnessite samples. The data were processed using the Noran System Six 3 (NSS 3) software.
210 Samples were initially prepared by putting carbon tape on top of an aluminum stub, and placing
211 the sample onto the tape for chemical analysis and imaging. Additional samples were also
212 prepared as polished sections using cold-set epoxy to avoid heating. Samples were not C coated,
213 and the EDS data were collected using the low-vacuum mode for chemical analysis.

214

215 **Electron probe microanalysis (EPMA)**

216 The polished sections of samples used for SEM/EDS were carbon coated for analysis on
217 an electron probe microanalyzer. A JEOL 8900 electron probe microanalyzer (Department of
218 Mineral Sciences, Smithsonian Institution) was used to determine chemical compositions. The
219 instrument was equipped with five wavelength-dispersive spectrometers (WDS), and was
220 operated at 15 kV accelerating voltage and 20 nA beam current. Electron probe point analyses
221 were collected for 15 elements using a 10 x 12 μm beam.

222 Chemical formulae for all birnessite samples are reported in Table 1. Note that for all
223 samples, EPMA measurements were complicated by the porous nature and lack of smooth, flat
224 surfaces due to small particle sizes and the flaky nature of the materials, making surface
225 polishing difficult during sample preparation. Consequently, weight percents often totaled to
226 ~60%, although the low totals in part resulted from uncertainties of Mn oxidation states (and

227 calculation of oxide weight composition), and the presence of significant amounts of water in the
228 birnessite structures (H_2O and OH). In general, the calculations of chemical formulas assumed
229 that all Mn had a valence of 4+, except for those samples that were analyzed by X-ray
230 photoelectron spectroscopy, which provided additional information regarding Mn oxidation
231 states.
232
233 **Fourier transform infrared spectroscopy (FTIR)**
234 Samples were disaggregated under acetone in a mortar and pestle and sieved through a
235 325 mesh sieve. Then, 0.5 to 1 mg of Mn oxide sample was milled with ~250 mg KBr using a
236 SPECAC ball mixing mill for 1-2 min, and pressed into a pellet. Transmission vibrational
237 spectra were collected on a Nicolet 6700 Analytical FTIR Spectrometer for a range of 400 to
238 4000 cm^{-1}. The resolution was set at 3.86 cm^{-1} and 64 scans were co-added for each spectrum.
239 The Omnic 8 software (Nicolet) was used to view data during data collection.
240
241 **X-ray absorption spectroscopy/extended X-ray absorption fine structure (XAS/EXAFS)**
242 For X-ray absorption spectroscopy, samples were ground under acetone in a mortar and
243 pestle, and sieved into a thin layer with a 425 or 500 mesh sieve onto Kapton® (polyimide) tape.
244 The Kapton tape was then folded to seal in the sample. Manganese *K*-edge XAS spectra were
245 collected using a synchrotron source at Beamline 12-BM of the Advanced Photon Source (APS),
246 Argonne National Laboratory using a Si(111) double-crystal, fixed exit monochromator and a
247 double mirror system (flat plus torroidal) with an energy cutoff of 23 keV. The pre-edge peak of
248 a Mn foil was used for energy calibration (6539 eV). Fluorescence data were collected with a 13-
249 element Ge detector with a Cr fluorescence Z-1 filter in front of the Ge detector to reduce the

contribution from elastic scattering. Three to six scans were collected per sample at room temperature from -200 eV to about +800 eV around the Mn *K*-edge (6539 keV). During data collection, the peak positions and line forms in the near edge region (XANES) were examined to check for photochemical reduction with successive scans, and no changes were observed.

Data analyses of spectra were conducted using the ATHENA software (Ravel & Newville 2005). XAS spectra were calibrated using a Mn foil, averaged, background-subtracted, normalized, and deglitched if outlier points were present. Analysis of the Mn *K*-edge EXAFS region was used for identification and phase fraction quantification of samples (Webb et al. 2005a, 2005b; Villalobos et al. 2006; Saratovsky et al. 2009; Feng et al. 2010). The χ(k) spectra were converted to k (Å^{-1}) (Sayers & Bunkers, 1988). The resulting data were k^2-weighted and analyzed using the k-range from 2.3 to 11.3 Å^{-1}.

Following previously reported practices, linear combination fitting (LCF) of the χ(k) spectra collected for natural phyllomanganates (or birnessite-like phases) yielded phase fractions of Mn oxides. The following standards were used to fit the EXAFS data: todorokite from South Africa (Smithsonian Insitution #NMNH R15434), romanechite from Van Horne, TX (Smithsonian Insitution #NMNH 97618), lithiophorite from South Africa (Smithsonian Insitution #NMNH 162391), cryptomelane from India (Smithsonian Insitution #NMNH 89104), chalcophanite from Sterling, NJ (Smithsonian Insitution #NMNH C1814), manganosite from Franklin, New Jersey (Smithsonian Insitution #NMNH #C6088), manganite from Germany (Smithsonian Insitution #NMNH 157872), manganese carbonate (Sigma-Aldrich), pyrolusite from Rossbach, Germany (Smithsonian Insitution #NMNH B6724), synthetic triclinic Na-birnessite, and synthetic pH 2 hexagonal birnessite. All weights were set between 0 and 1, and all combinations were fit with at most 3 standards. Principal component analysis (PCA) was

used to determine the number of components representing the entire data set (Manceau et al. 2002) with results shown in SI Table 1. Target transformations were used to evaluate the fitness of each reference sample to the data set. LCF of the X-ray absorption near-edge structure (XANES) region were also performed to determine the Mn oxidation states of samples using manganese carbonate, manganite, and pyrolusite standards.

In a separate analysis, to determine a sample's resemblance to synthetic triclinic and/or synthetic hexagonal birnessite, only synthetic triclinic Na-birnessite and synthetic pH 2 hexagonal birnessite were used in the LCF. Todorokite was included as a third phase in the analysis only if XRD indicated that it was present. Weights of standards were not forced to sum to 1.

X-ray photoelectron spectroscopy (XPS)

For XPS analysis, data collection and fitting procedures were followed as reported by Ilton et al. (2016). Powder samples were mounted on strips of conductive copper tape affixed to copper stubs and then pressed with clean borosilicate glass blocks onto copper stubs. Measurements were conducted with a Kratos Axis Ultra DLD spectrometer with an Al $K\alpha$ X-ray source (1486.7 eV) operating at 10 mA and 15 kV. Magnetic immersion lenses were used to improve collection efficiency. The instrument work function was calibrated to give a binding energy (BE) of 83.96 eV ± 0.05 eV for the $4f_{7/2}$ line of metallic gold. The spectrometer dispersion was adjusted to yield a BE of 932.62 eV for the Cu$2p_{3/2}$ line of metallic copper. Measurements of the Mn*2p*, Mn*3s*, Mn*3p*, O*1s*, C*1s*, and various alkali and alkaline Earth lines were conducted with a step size of 0.1 eV, an analysis area of 300 x 700 μm, and pass energies (PE) of 20 or 40 eV. The resultant full-width-at-half-maximums (FWHM) for the Ag$3d_{5/2}$ line

were 0.54 and 0.77 eV, respectively. The low sensitivity of the Mn*3s* line resulted in measurements only with PE = 40 eV. Survey scans were conducted at PE = 160 eV and step size = 0.5 eV. XPS spectra were fit by non-linear least squares after Shirley background subtractions with the CasaXPS curve resolution software package. Gaussian/Lorentzian contributions to line shapes were numerically convoluted with a Voigt function.

RESULTS AND DISCUSSION

Comparison of natural birnessites to "δ-MnO_2"

We sought to determine whether the extreme turbostratic disorder observed in lab biomineralizations of MnO_2 was characteristic of birnessites in terrestrial, freshwater systems. Villalobos et al. (2003) analyzed Mn oxides precipitated by cultures of the bacterium *Pseudomonas putida* strain MnB1 as an analog for birnessite-like phases produced biogenically in soils and fresh water environments. These experiments consistently yielded vernadite-like nanoparticles. Vernadite is a birnessite-like phase that is either disordered in the layer stacking direction, or consists of crystallites with so few MnO_6 layers that powder XRD patterns show no basal reflections (Bricker 1965; Giovanoli & Arrhenius 1988). The term "δ-MnO_2", often used to distinguish birnessite from other MnO_2 polymorphs, typically is used more restrictively in the environmental geochemistry literature to denote a poorly crystalline biogenic vernadite.

The laboratory-produced biogenic birnessites generated diffuse X-ray diffraction patterns with weak or absent 001 and 002 reflections, suggesting to those authors that the nanoparticles contained only a few randomly stacked sheets per particle like vernadite. For comparison, we examined our samples first using conventional (Mo K_α) X-ray diffraction. In a striking difference from lab-cultured δ-MnO_2, all eleven XRD patterns of the natural samples exhibited

prominent 10 Å or 7 Å basal reflections (Fig. 2, 4). Whereas some patterns seemed to match that of hexagonal ranciéite, others were less interpretable "3-line" birnessite varieties. The natural ranciéite-like samples included specimens from Paxton Cave, VA, Granada, Spain, and the French Pyrenees (Fig. 2). SEM images of specimens from France and Spain showed flake-like crystals that measured ~100 μm in diameter but were only tens of nanometers thick (Fig. 3). The Paxton Cave sample, on the other hand, appeared as fluffy orbicules of birnessite mixed with diatoms (Fig. 3b). EPMA analyses revealed that Ca was the dominant interlayer cation in all three of these samples, although a host of other metals, including Mg, Fe, Zn, Al, Ba, K, Na and possibly Si, also were observed in various samples above trace concentrations (Table 1). As the natural birnessite samples sometimes were intergrown with aluminum silicate, assumed to be kaolinite, Al and Si may have originated from aluminosilicate clays that fell below the EPMA imaging resolution.

The diffraction patterns for the remaining natural samples showed 3 broad, relatively asymmetric peaks in their XRD patterns (so-called "3-line birnessite") with d-spacings of ~7.2 Å, ~2.4 Å, and ~1.4 Å (Fig. 4). The XRD patterns for the sample from Spring Branch, TN and three from central Pennsylvania (DS1-M3f, DS2-M3f, and PBS-M2f-2) exhibited a 10 Å basal d-spacing, indicating buserite-like structures (SI Fig. 4); these were dried at 110°C to collapse the layer spacing to 7 Å to confirm that they were layer phases (and not todorokite) and to allow a more direct comparison with other natural 7 Å phases. Interestingly, one of the central Pennsylvanian samples (PBS-M2f-1) that exhibited a 10 Å d-spacing failed to collapse completely upon heating. However, linear combination fitting of EXAFS did not identify any todorokite in this sample that might produce the 10 Å spacing observed by XRD. Ca^{2+}, Mg^{2+}, Ni^{2+}, and Co^{2+} cations have been observed to stabilize the buserite structure, and both Ca^{2+} and

342 Mg^{2+} were detected by EPMA in these samples (Table 1). It still is unclear why some buserites
343 fully collapse upon heat treatment at 110°C, while others do not.

344 In SEM images, the "3-line" birnessite samples consisted typically of flake-like crystals
345 that measured <10 μm across, somewhat similar to the crystal habits observed in the Paxton
346 Cave sample, but commonly the "3-line" birnessites were agglomerated into fluffy spherules
347 measuring ~10 to ~20 μm in diameter (Fig. 5a – 5c). Diatoms were commonly observed
348 associated with the "3-line" birnessite spherules, but any role that the diatoms may have played
349 in the precipitation of the Mn oxide phases is not clear. Additional SEM images of the natural
350 birnessites are presented in SI Fig. 5.

351 As all of the natural "3-line" birnessite samples shown in Fig. 5 were associated with
352 limestone/dolomite-lined streambeds or Fe/Mn treatment systems, with the exception of the
353 sample from Lake Vermilion, it is not surprising that the major cations detected by EPMA
354 analyses included Ca, Mg, and Fe (Table 1). The Al and Si, as mentioned above, were likely
355 associated with aluminosilicate clays intergrown with the Mn oxides, as shown in Fig. 5c and 5e.
356 In the lake nodule from Vermilion, MN, Ba was the dominant cation after Mn (Table 1). We
357 presume that Ba, Ca and Mg are located in the interlayer, based on numerous birnessite synthesis
358 and exchange studies (Golden et al. 1987; Post & Veblen 1990; Lopano et al. 2007). Additional
359 presumed interlayer cations detected in various natural "3-line" birnessite specimens included
360 Zn, K, and Na. Some analyses also detected Cu, which likely substitutes into the octahedral
361 sheets (e.g., Manceau et al. 1992).
362

363 **Local structure of "3-line" birnessites using EXAFS**

Although XRD analysis confirmed that the "3-line" Mn oxide samples were members of the birnessite family, the limited number of peaks in these patterns and peak asymmetry indicate a degree of structural disorder that cannot be modeled by routine Rietveld analysis methods. Consequently, XRD alone could not definitively distinguish these samples as triclinic or hexagonal, or some mixture of the two. Previous researchers have employed linear combination fitting (LCF) of EXAFS spectra, which are sensitive to local structure, as one strategy to characterize poorly crystalline birnessite-like samples (Tan et al. 2010; Learman et al. 2011, 2013; Santelli et al. 2011; Zhao et al. 2016).

Previous studies have concluded that in χ(k) plots generated from EXAFS data, a single, sharp antinode at ~8.2 $Å^{-1}$ is indicative of hexagonal birnessite whereas a positive double antinode at ~8.0 $Å^{-1}$ is indicative of triclinic birnessite (Webb et al. 2005a). These features are clearly visible in the EXAFS data for our synthetic hexagonal H-birnessite and triclinic Na-birnessite (Fig. 6). Among our "3-line" birnessite samples, analysis of the χ(k) plots at 8.2 $Å^{-1}$ suggests that most samples have features that lie between those of the triclinic and hexagonal birnessite end-members, as is consistent with the analyses of birnessites associated with acid-mine treatment sites described in Tan et al. (2010) (Fig. 6). The laboratory cultured fungal produced specimen (labeled Stag50Ca1.5Mn) exhibited the sharpest distinct peak at ~8.2 $Å^{-1}$, suggesting that its structure is close to that of hexagonal birnessite. On the other hand, the samples from Spring Branch, TN and from a central Pennsylvania treatment site (PBS-M2f-2) displayed a double antinode at ~8.2 $Å^{-1}$ suggesting that they consist primarily of triclinic birnessite phases (Fig. 6). Although the double antinodes in the "3-line" birnessite samples were not as obvious as those in synthetic triclinic Na-birnessite, the overall features at 8.2 $Å^{-1}$ in these samples contrast to the single, well-defined peak from synthetic hexagonal H-birnessite.

This is a preprint, the final version is subject to change, of the American Mineralogist (MSA)
Cite as Authors (Year) Title. American Mineralogist, in press.
DOI: https://doi.org/10.2138/am-2020-7303

Other features in the χ(k) spectra also can be suggestive of either triclinic or hexagonal character. As the apparent "hexagonality" of a sample increases, the match for the shapes and intensities of the peaks at ~7.0 and at ~9.3 $Å^{-1}$ in the χ(k) plots improved relative to those observed for the synthetic hexagonal H-birnessite (Fig. 6). By contrast, the shapes and intensities for the ~7.0 $Å^{-1}$ and ~9.3 $Å^{-1}$ peaks for natural samples with a highly triclinic character matched better for those in the χ(k) spectrum of synthetic triclinic birnessite than for the hexagonal H-birnessite.

According to McKeown and Post (2001), the 6.8, 8.0, and 9.3 $Å^{-1}$ peaks in the χ(k) plots are sharper and have higher amplitudes for layer structures like birnessite than for tunnel structures like todorokite. The dampening of these peaks in todorokite is attributed to the 4 symmetrically distinct Mn sites in todorokite, giving rise to slightly different local environments for Mn, in contrast to the single symmetrically distinct Mn site in ideal hexagonal birnessite. Modeling by Webb et al. (2005a) showed that the double antinode at ~8.0 $Å^{-1}$ in triclinic birnessites is a consequence of out-of-plane bending in the Mn octahedral sheet. We extend the above interpretations to our data to suggest that peak dampening and shifts toward higher wavenumbers, especially for the 6.8 and 9.3 $Å^{-1}$ peaks, can be attributed to Jahn-Teller distortions associated with increased Mn^{3+} concentrations, and thus increasing triclinicity in birnessite (Ling et al. 2018).

Overall, the total radial distribution functions (RDFs) of "3-line" birnessite samples matched those generated from the synthetic hexagonal and triclinic birnessites to varying degrees (Fig. 7). The RDFs generated for the Spring Branch, TN and central Pennsylvanian DS2-M3f samples matched that of triclinic Na-birnessite over the range of 4 to 5 Å. Likewise, the RDFs produced by the fungal Stag50Ca1.5Mn and the central Pennsylvanian DS1-M3f and Glasgow

410 samples matched those for synthetic hexagonal birnessite reasonably well in the range 4.3 to 5.7
411 Å. Other regions of the RDFs yielded noticeable differences between the "3-line" birnessites and
412 the synthetic triclinic or hexagonal birnessites.
413
414 **LCF analysis of EXAFS spectra for natural birnessites**
415 One aim of the present study was to determine whether the natural birnessites associated
416 with freshwater, terrestrial systems could be identified as having either hexagonal or triclinic
417 symmetry, since birnessite reactivity is so strongly correlated with crystal chemistry and
418 structure. The EXAFS spectra generated by the natural birnessite samples analyzed in this study
419 were similar overall to those from the synthetic hexagonal and triclinic birnessite standards when
420 analyzed with the subset of references determined from target transformations. As mentioned
421 above, it has also been a common practice to apply linear combination fitting (LCF) methods
422 using Mn oxide standards to determine the relative amounts of triclinic and hexagonal
423 constituents in birnessite samples. Therefore, we applied LCF analysis to the EXAFS spectra
424 generated by the three samples that our XRD patterns indicated are hexagonal ranciéite-like
425 phases – the samples from France, Spain, and Paxton Cave, VA. Because minor amounts of
426 todorokite were identified with XRD in addition to the ranciéite-like phase in these samples,
427 LCF was conducted with 3 standards: todorokite, synthetic triclinic Na-birnessite, and synthetic
428 pH 2 hexagonal birnessite. The ranciéite samples were not included as a standard due to
429 todorokite impurities as indicated by XRD.
430 To our surprise, LCF analyses for these specimens yielded significant fractions of
431 triclinic birnessite in these hexagonal samples, ranging from 15±4 vol% (Paxton Cave, VA) to
432 19±5 vol% (France Pyrenees) triclinic birnessite (Table 2). As the XRD patterns for these three

433 samples can be well fit using only a single hexagonal birnessite structure with Rietveld
434 refinement (Post et al. 2008), the LCF result might be explained in several ways. One
435 interpretation is that the Rietveld refinements did not detect an existing minor triclinic phase.
436 Although possible, our refinements routinely reveal even 5-10% triclinic birnessite in standard
437 hexagonal/triclinic mixtures. Alternatively, the natural samples might contain triclinic birnessite
438 intergrowths at a length scale that falls below the correlation distance of X-ray diffraction, on the
439 order of 10 unit cells, or ~7 nm along the *c* axis direction. We are skeptical of this interpretation
440 based on our XPS analyses of some of these same samples (Ilton et al. 2016). For example, XPS
441 results for the ranciéite from Paxton Cave, VA yielded a higher fraction of Mn^{4+} (91 mol%) and
442 no Mn^{3+} (0 mol%), less than even our hexagonal H-birnessite standard. As the Jahn-Teller
443 distortions associated with Mn^{3+} drive the departure from hexagonal symmetry (Silvester et al.
444 1997; Drits et al. 1997), it seems unreasonable that a birnessite specimen with little or no Mn^{3+}
445 would exhibit significant triclinic character.
446 Perhaps the most likely explanation for the discrepancies observed between powder X-
447 ray diffraction and LCF analysis of EXAFS data arise from the use of standard birnessite end-
448 members in the linear combination fitting, neither of which matches the compositions, or precise
449 structures, of possible phases making up the natural samples. Synthetic H-birnessite is different
450 from ranciéite, and presumably from the other natural samples studied here. In natural ranciéite,
451 Ca is the dominant inter-layer cation, as was seen in the Paxton Cave and our other natural
452 samples, whereas the interlayer cations for H-birnessite are Mn^{2+} (and perhaps Mn^{3+}) and
453 possibly H^{+}. The interlayer cation in our standard triclinic birnessite is Na^{+}, which again is
454 different than for any of our natural samples. Additionally, XPS data given here and in previous
455 studies (Ilton et al. 2016) reveal a range of Mn oxidation state profiles for synthetic and natural

This is a preprint, the final version is subject to change, of the American Mineralogist (MSA)
Cite as Authors (Year) Title. American Mineralogist, in press.
DOI: https://doi.org/10.2138/am-2020-7303

phyllomanganates, even for nominally hexagonal birnessite-like phases, and even when the average Mn oxidation states are similar. Variations of Mn^{4+}/Mn^{3+} values will affect the unit-cell and other parameters of the birnessite structure, and if those ratios are different for standard phases than for the samples being characterized, errors will accompany the LCF analyses. We attempted to synthesize hexagonal Ca-birnessite that is similar to ranciéite to explore its use as an endmember for LCF analysis, but our efforts have not been successful. We propose that the disparities in the EXAFS spectra of synthetic H-birnessite and natural Ca-rich hexagonal birnessites are compensated in the LCF procedure through the incorporation of triclinic Na-birnessite.

Moreover, we also question the use of synthetic triclinic Na-birnessite as an analog for most natural birnessites from freshwater environments. Ling et al. (2018) showed that synthetic birnessites with different interlayer cations have structural characteristics that fall between those of hexagonal H-birnessite and triclinic Na-birnessite. For example, the powder X-ray diffraction pattern for a synthetic triclinic Ca-birnessite was best fit, using Rietveld methods, with a mixture of 59.4 vol% hexagonal and 40.6 vol% triclinic birnessite. In natural non-marine birnessite samples that can have several different interlayer cations, is it appropriate to use synthetic triclinic Na-birnessite (or K-birnessite) as one endmember of an LCF analysis, especially when the natural sample contains little or no Na? Although Na was the dominant interlayer cation in the type birnessite from Birness, Scotland (Jones and Milne 1956), EPMA of our natural samples indicated that Na, although sometimes present, was never the dominant cation (Table 1). The complexity of natural birnessite-like Mn oxides suggests that LCF of EXAFS spectra using synthetic endmember compositions may not accurately assess the degree of hexagonality and triclinicity, particularly if the fits are done without appropriate reference mineral spectra. In

addition, LCF analysis does not differentiate a mixture of hexagonal and triclinic phases and a single phase that is structurally intermediate between the endmember triclinic and hexagonal standards. Instead of LCF analysis, full modeling of the local Mn coordination environment, such as the complete models for biogenically produced Ca-birnessites and Na-birnessite (Webb et al. 2005a, 2005b; John R. Bargar et al. 2009; Santelli et al. 2011; Hinkle et al. 2016), might be the most accurate method of determining the specific birnessite structures of natural Mn oxide minerals from XAS data.

Distinguishing the symmetry of natural birnessites by FTIR spectroscopy

Although XRD readily identified some of our natural birnessites as hexagonal, it provided only limited information for the "3-line" birnessites. LCF of EXAFS suggested that these 3-line birnessites contained a mixture of triclinic and hexagonal birnessite, but as discussed above, there are limitations to quantification of triclinic and hexagonal birnessite using LCF. Ling et al. (2016) showed that Fourier transform infrared spectroscopy (FTIR) is sensitive to differences between synthetic triclinic and hexagonal birnessite, particularly within the 400 to 750 cm^{-1} Mn-O bond stretching region. Like EXAFS and unlike XRD, FTIR probes short-range atomic interactions, and it may provide a more accurate characterization of mixtures of triclinic and hexagonal birnessite in synthetic samples than LCF of EXAFS.

Our FTIR analyses of the ranciéite-like natural samples confirmed their structures as purely hexagonal birnessites, in agreement with our XRD and XPS results. As with synthetic hexagonal H-birnessite, the FTIR spectra produced by the specimens from France, Spain, and Paxton Cave, VA exhibited two distinct peaks -- at ~426 cm^{-1} and ~493 cm^{-1} (Fig. 11, Table 3), and peaks were sharper for the natural hexagonal birnessites from Spain and France than for the

synthetic H-birnessite standard. The sample from Paxton Cave, VA yielded broad peaks due to an additional weak peak at 456 cm^{-1}, which likely represented an Si-O band from inclusions of diatoms and/or quartz. The full FTIR spectra for all natural samples can be found in SI Fig. 6.

The FTIR provided insights into the "3-line birnessites" that could not be clearly identified as triclinic or hexagonal using XRD. Samples from Spring Branch, TN and from central Pennsylvania (PBS-M2f-1, PBS-M2f-2, and DS2-M3f) exhibited three distinct peaks that clearly resembled those associated with synthetic triclinic Na-birnessite: at ~431, ~472, and ~510 cm^{-1} (Fig. 12, Table 3). However, the natural sample peaks were broader, perhaps because of poor crystallinity, or the presence of some hexagonal birnessite, or both. These samples initially were all buserites. After dehydration at 110°C, the FTIR spectra remained unchanged in the 400 to 750 cm^{-1} range (Fig. 13), despite evidence by XRD of structural collapse, with the exception of PBS-M2f-1, which did not fully collapse (SI Fig. 7). The central Pennsylvanian DS1-M3f sample, also a buserite, somewhat resembled triclinic birnessite initially in the FTIR spectra with broad peaks at 431, 468, and 498 cm^{-1}, but appeared more hexagonal after dehydration, perhaps from the broadening related to increased structural disorder, and merging, of the peaks at 431 and 468 cm^{-1} (Fig. 13). A birnessite sample from a different remediation site in Pennsylvania, labeled as Glasgow, and the fungally precipitated synthetic sample, labeled as Stag50Ca1.5Mn, yielded peaks at ~447 and ~496 cm^{-1} that closely resembled those of synthetic hexagonal H-birnessite (Fig. 12, Table 3). The FTIR spectra in Fig. 12 are ordered according to their general resemblance to synthetic triclinic (top) or synthetic hexagonal birnessite (bottom).

Although FTIR was able to differentiate the overall hexagonal and triclinic character of natural birnessites with greater clarity than did LCFs of EXAFS, the broad peaks challenged our efforts at quantification. Even recognizing the limitations, however, it is possible that the

525 fractions of triclinic and hexagonal birnessite determined from LCF of EXAFS spectra (Table 2)
526 might provide some insights for better interpreting the FTIR spectra. If we order the FTIR
527 spectra for the "3-line" birnessites based on the degree of hexagonal character as suggested by
528 our LCF analyses of the EXAFS spectra, we observe consistent shifts in the peak positions,
529 particularly for peak 3 (Fig. 14, Table 3). Peak 3 (Fig. 14) shifts from 514 to 496 cm^{-1} as the
530 amount of hexagonal character in the sample increases. However, we note that in general, LCF
531 analysis of the FTIR spectra confronts the same limitations as does LCF analysis of EXAFS
532 data: using synthetic triclinic Na-birnessite and synthetic hexagonal H-birnessite for the spectral
533 unmixing of FTIR peaks, as described for synthetic samples by Ling et al. (2016), is
534 inappropriate for natural samples.
535
536 **Relationship between Mn oxidation state and crystal structure of natural birnessites**
537 XPS was applied to a subset of the natural samples examined in the present study in order
538 to determine Mn oxidation states (Ilton et al. 2016), and a direct correlation between Mn^{3+}
539 concentration and the fraction of triclinic birnessite, as ascertained from EXAFS and FTIR, was
540 observed. For example, XPS analysis of the natural birnessite from Spring Branch, TN yielded
541 37 mol% Mn^{3+} (Fig. 10), comparable to our synthetic triclinic Na-birnessite (with 38 mol%
542 Mn^{3+}). Both EXAFS and FTIR analyses indicated a high degree of triclinicity for this sample
543 (Fig. 6, 12). At the opposite end of the spectrum, XPS analysis of the central Pennsylvanian
544 Glasgow sample yielded only 23 mol% Mn^{3+}, within error of the value for our synthetic
545 hexagonal H-birnessite (with 22 mol% Mn^{3+}). As previously noted, the sample from Paxton
546 Cave, VA contained the lowest concentration of Mn^{3+} of any samples that we analyzed by XPS
547 (0 mol% Mn^{3+}), and the XRD (Fig. 2) and FTIR (Fig. 11) analyses indicated that this sample is

548 purely hexagonal. In fact, the Mn-O stretching vibrations for the Paxton Cave, VA sample as
549 revealed by the FTIR data were shifted to even lower wavenumbers than was observed in
550 synthetic hexagonal H-birnessite. Whereas our synthetic hexagonal H-birnessite standard
551 yielded IR peaks at 447 and 496 cm^{-1}, the Paxton Cave, VA sample exhibited corresponding
552 vibrations at 426 and 492 cm^{-1} (Fig. 11, Table 3).

553 These results are consistent with our conclusions in a study of cation-exchanged synthetic
554 birnessites (Ling et al. 2018) that FTIR peak positions may provide an estimate for Mn oxidation
555 state ratios. By contrast, LCF analyses of EXAFS spectra seem less reliable than FTIR, given
556 that the "very triclinic" Spring Branch, TN sample (37 mol% Mn^{3+}) was fitted as 56 vol%
557 triclinic Na-birnessite and 44 vol% hexagonal H-birnessite, and the "very hexagonal" Glasgow
558 sample (22 mol% Mn^{3+}) was fitted as 24 vol% triclinic Na-birnessite and 78 vol% hexagonal H-
559 birnessite. For samples that contained >57 vol% hexagonal H-birnessite, when fitting all
560 possible combinations with LCF and limiting the fit to 2 standards, best results were achieved
561 when either chalcophanite or cryptomelane were included. However, XRD showed no indication
562 of cryptomelane and chalcophanite. The inclusion of chalcophanite was likely due to its
563 structural resemblance to hexagonal birnessite as a layered Mn oxide, but with all Mn^{4+} in the
564 octahedral sheet and Zn^{2+} ions in the interlayer.

565 Analyses of the XANES region using LCF yielded Mn oxidation state ratios comparable
566 to XPS values within ±5% (SI Table 2), with the exception of the Spring Branch sample that
567 yielded values within ±17%. The high Mn^{3+} content of the Spring Branch sample relative to the
568 other birnessites may have led to the differences in oxidation state values between the two
569 techniques. Likewise, Chalmin et al. (2009) and Manceau et al. (2012) report difficulties in
570 determining Mn oxidation state ratios through basic LCF of the XANES region of XAS data for

This is a preprint, the final version is subject to change, of the American Mineralogist (MSA)
Cite as Authors (Year) Title. American Mineralogist, in press.
DOI: https://doi.org/10.2138/am-2020-7303

571 mixed-valence Mn oxides with more than 2 Mn oxidation states present. Furthermore, LCF of
572 this region is highly dependent on the selection of reference standards. For example, the use of a
573 natural manganosite as the reference for Mn^{2+} as opposed to the synthetic manganese carbonate
574 yielded values within ±25% of the XPS values.

575 If we plot the peak positions in the 400 to 750 cm^{-1} range for the samples in which we
576 have XPS data in the same manner as for Fig. 14, we find that as Peak 3 shifts from 496 to 514
577 cm^{-1}, Mn^{3+}/Mn_{total} also increases, yielding a linear fit with an R^2 value of 0.82 (Fig. 15). The
578 relationship between the fraction of Mn^{3+} and the position of Peak 3 can be described as:

579 $$P_3 = 56.8X_{Mn^{3+}} + 488.8 \quad (1)$$

580 where P_3 is the Peak 3 position in the FTIR spectra and $X_{Mn^{3+}}$ is the molar fraction of Mn^{3+}
581 (Mn^{3+}/Mn_{total})

582

583 **Structural differences in birnessite samples with similar formation environments**

584 One of the most surprising conclusions of the present study is that birnessite minerals that
585 formed in ostensibly very similar environments can exhibit dramatically different crystal
586 chemistries. We included several samples from mine remediation sites having analogous designs
587 in central Pennsylvania. The samples labeled as Glasgow, DS1-M3f, DS2-M3f, PBS-M2f-1, and
588 PBS-M2f-2 all formed at ambient temperatures in run-off waters from Appalachian coal wastes
589 that were enriched in Mn^{2+} (Tan et al. 2010; Santelli et al. 2011; Luan et al. 2012). As a result of
590 acid neutralization by limestone cobbles in the passive treatment systems, dissolved Mn^{2+} was
591 likely oxidized by a combination of microbiological activity and surface-catalyzed
592 heterogeneous oxidation on $Mn^{3+,4+}$ oxide surfaces (Davies & Morgan 1989; Junta & Hochella
593 1994).

When examined by SEM, these precipitates all appeared as flakey spherules measuring <10 μm in diameter (Fig. 5), and XRD of all these samples yielded "3-line" birnessite patterns. Thus, by many of the techniques conventionally used to characterize minerals in the environment, these samples were indistinguishable. When XPS, EXAFS and FTIR were all applied to these birnessite-like precipitates, however, variations in Mn oxidation state ratios and in degree of triclinic and hexagonal character emerged without ambiguity. These samples displayed a range of structures from highly triclinic (DS2-M3f) to hexagonal (Glasgow), with other samples from the same sites falling in between (Fig. 12). We infer that subtle differences in solution chemistry, organic activity, and temperature can affect the Mn oxidation state and the variety of birnessite that forms.

IMPLICATIONS

In this largest study of nonmarine birnessites to date, we observed a variety of birnessites that differed with respect to crystallographic phase, particle size, interlayer cations, and Mn oxidation state ratios. Both triclinic and hexagonal varieties were detected in these natural samples, although it is unclear whether the varieties grew as interlayered endmembers or whether the mixed composites exhibited structures that are intermediate between the endmembers.

Our previous study used FTIR to differentiate between various synthetic analogues of birnessite (Ling et al. 2018), and here we demonstrated that FTIR can successfully yield information concerning natural birnessites. The insights provided by FTIR are even more robust when combined with XPS, which allows for the complementary determination of Mn oxidation state ratios, and chemical analyses. The observed correlation between the XPS and FTIR analyses of natural samples reveals that FTIR data can be used to determine Mn^{3+} content. Our

617 results support the observations of Tan et al. (2010) that triclinic birnessite is abundant in natural
618 samples.
619
620 **ACKNOWLEDGMENTS**

621 Funding for this work was provided by NSF Grant EAR-1147728 and EAR-1552211 and
622 the Committee on Institutional Cooperation (CIC) and Smithsonian Institution Fellowship. This
623 research also utilized samples from the Smithsonian Mineral Research Collection at the Museum
624 of Natural History. The FTIR laboratory at the Smithsonian Institution was established with
625 generous support from Stephen Turner. This research used resources of the Advanced Photon
626 Source, a U.S. Department of Energy (DOE) Office of Science User Facility operated for the
627 DOE Office of Science by Argonne National Laboratory under Contract No. DE-AC02-
628 06CH11357. ESI is supported by the PNNL managed Geosciences Research Program of the
629 U.S. Department of Energy (DOE), Office of Basic Energy Sciences, Division of Chemical
630 Sciences, Geosciences & Biosciences. The research was performed in part using the
631 Environmental Molecular Sciences Laboratory (EMSL), a national scientific user facility
632 sponsored by the U.S. DOE's Office of Biological and Environmental Research and located at
633 Pacific Northwest National Laboratory (PNNL). PNNL is operated for DOE by Battelle
634 Memorial Institute under Contract# DE-AC06-76RLO-1830. Special thanks David McKeown
635 for his help with learning XAS, to Alexandre Fowler for her contribution to data collection, to
636 Carla E. Rosenfeld for her preparation of the fungal birnessite, to Margaret A.G. Hinkle for her
637 help with LCF, and to Michael Sommers for his donation of samples from Lake Vermilion.

REFERENCES

Allard, S., Gutierrez, L., Fontaine, C., Croué, J. P., & Gallard, H. (2017). Organic matter interactions with natural manganese oxide and synthetic birnessite. *Science of the Total Environment*, *583*, 487–495. https://doi.org/10.1016/j.scitotenv.2017.01.120

Bargar, J.R., Tebo, B. M., Bergman, U., Webb, S. M., Glatzel, P., Chiu, V. Q., & Villalobos, M. (2005). Biotic and abiotic products of Mn(II) oxidation by spores of the marine Bacillus sp. strain SG-1. *American Mineralogist*, *90*, 143–154. https://doi.org/10.2138/am.2005.1557

Bargar, John R., Fuller, C. C., Marcus, M. A., Brearley, A. J., Perez De la Rosa, M., Webb, S. M., & Caldwell, W. A. (2009). Structural characterization of terrestrial microbial Mn oxides from Pinal Creek, AZ. *Geochimica et Cosmochimica Acta*, *73*, 889–910. https://doi.org/10.1016/j.gca.2008.10.036

Bartlett, R. J., & James, B. (1979). Behavior of Chromium in Soils: III. Oxidation. *Journal of Environment Quality*, *8*(1), 31–35. https://doi.org/10.2134/jeq1976.00472425000500040010x

Bilinski, H., Giovanoli, R., Usui, A., & Hanzel, D. (2002). Characterization of Mn oxides in cemented streambed crusts from Pinal Creek , Arizona , U.S.A., and in hot-spring deposits from Yuno-Taki Falls , Hokkaido , Japan. *American Mineralogist*, *87*, 580–591.

Bricker, O. (1965). Some Stability Relations in the System Mn-O2-H2O at 25˚ and One Atmosphere Total Pressure. *The American Mineralogist*, *50*, 1296–1354.

Chalmin, E., Farges, F., & Brown, G. E. (2009). A pre-edge analysis of Mn K-edge XANES spectra to help determine the speciation of manganese in minerals and glasses. *Contributions to Mineralogy and Petrology*, *157*, 111–126. https://doi.org/10.1007/s00410-008-0323-z

661 Chao, T. T., & Theobald, P. K. (1976). The significance of secondary iron and manganese oxides
662 in geochemical exploration. *Economic Geology*, *71*, 1560–1569.
663 https://doi.org/10.2113/gsecongeo.71.8.1560
664 Davies, S. H. R., & Morgan, J. J. (1989). Manganese (II) Oxidation Kinetics on Metal Oxide
665 Surfaces. *Journal of Colloid & Interface Science*, *129*(1), 63–77.
666 Drits, V. A., Silvester, E., Gorshkov, A. I., & Manceau, A. (1997). Structure of synthetic
667 monoclinic Na-rich birnessite and hexagonal birnessite: II. Results from chemical studies
668 and EXAFS spectroscopy. *American Mineralogist*, *82*(9–10), 962–978.
669 Fandeur, D., Juillot, F., Morin, G., Olivi, L., Cognigni, A., Webb, S. M., … Brown, G. E. (2009).
670 XANES evidence for oxidation of Cr(III) to Cr(VI) by Mn-oxides in a lateritic regolith
671 developed on serpentinized ultramafic rocks of New Caledonia. *Environmental Science &*
672 *Technology*, *43*, 7384–7390. Retrieved from
673 http://www.ncbi.nlm.nih.gov/pubmed/19848150
674 Feng, X. H., Zhu, M., Ginder-Vogel, M., Ni, C., Parikh, S. J., & Sparks, D. L. (2010). Formation
675 of nano-crystalline todorokite from biogenic Mn oxides. *Geochimica et Cosmochimica*
676 *Acta*, *74*, 3232–3245. https://doi.org/10.1016/j.gca.2010.03.005
677 Fleeger, C. R., Heaney, P. J., & Post, J. E. (2013). A time-resolved X-ray diffraction study of Cs
678 exchange into hexagonal H-birnessite. *American Mineralogist*, *98*, 671–679.
679 Frierdich, A. J., Hasenmueller, E. a., & Catalano, J. G. (2011). Composition and structure of
680 nanocrystalline Fe and Mn oxide cave deposits: Implications for trace element mobility in
681 karst systems. *Chemical Geology*, *284*(1–2), 82–96.
682 https://doi.org/10.1016/j.chemgeo.2011.02.009
683 Giovanoli, R., & Arrhenius, G. (1988). *The Manganese Nodule Belt of the Pacific Ocean*. (P.

684 Halbach, G. Friedrich, & U. von Stackelberg, Eds.).
685 Golden, D. C., Chen, C. C., & Dixon, J. B. (1986). Synthesis of todorokite. *Science (New York,*
686 *N.Y.)*, *231*(4739), 717–719. https://doi.org/10.1126/science.231.4739.717
687 Golden, D. C., Chen, C. C., & Dixon, J. B. (1987). Transformation of birnessite to buserite,
688 todorokite, and manganite under mild hydrothermal treatment. *Clays and Clay Minerals*,
689 *35*(4), 271–280.
690 Hansel, C. M., Zeiner, C. A., Santelli, C. M., & Webb, S. M. (2012). Mn(II) oxidation by an
691 ascomycete fungus is linked to superoxide production during asexual reproduction.
692 *Proceedings of the National Academy of Sciences*, *109*(31), 12621–12625.
693 https://doi.org/10.1073/pnas.1203885109
694 Hinkle, M. A. G., Flynn, E. D., & Catalano, J. G. (2016). Structural response of
695 phyllomanganates to wet aging and aqueous Mn(II). *Geochimica et Cosmochimica Acta*,
696 *192*, 220–234. https://doi.org/10.1016/j.gca.2016.07.035
697 Ilton, E. S., Post, J. E., Heaney, P. J., Ling, F. T., & Kerisit, S. N. (2016). XPS determination of
698 Mn oxidation states in Mn (hydr)oxides. *Applied Surface Science*, *366*, 475–485.
699 https://doi.org/10.1016/j.apsusc.2015.12.159
700 Johnson, K., Purvis, G., Lopez-Capel, E., Peacock, C., Gray, N., Wagner, T., … Greenwell, C.
701 (2015). Towards a mechanistic understanding of carbon stabilization in manganese oxides.
702 *Nature Communications*, (May). https://doi.org/10.1038/ncomms8628
703 Junta, J. L., & Hochella Jr., M. F. (1994). Manganese (II) oxidation at mineral surfacees A
704 microscopic and spectroscopic study. *Geochimica et Cosmochimica Acta*, *58*(22), 4985–
705 4999.
706 Jürgensen, A., Widmeyer, J. R., Gordon, R. A., Bendell-Young, L. I., Moore, M. M., & Crozier,

707 E. D. (2004). The structure of manganese oxide on the sehath of the bacterium Leptothrix
708 discophora: An XAFS study. *American Mineralogist*, *89*, 1110–1118.
709 Kay, J. T., Conklin, M. H., Fuller, C. C., & O'Day, P. A. (2001). Processes of nickel and cobalt
710 uptake by a manganese oxide forming sediment in Pinal Creek, Globe mining district,
711 Arizona. *Environmental Science & Technology*, *35*(24), 4719–4725. Retrieved from
712 http://www.ncbi.nlm.nih.gov/pubmed/11775144
713 Kazakis, N., Kantiranis, N., Voudouris, K. S., Mitrakas, M., Kaprara, E., & Pavlou, a. (2015).
714 Geogenic Cr oxidation on the surface of mafic minerals and the hydrogeological conditions
715 influencing hexavalent chromium concentrations in groundwater. *Science of The Total*
716 *Environment*, *514*, 224–238. https://doi.org/10.1016/j.scitotenv.2015.01.080
717 Kong, K. P., Fischer, T. B., Heaney, P. J., Post, J. E., Stubbs, J. E., & Eng, P. J. (2019).
718 Mineralogical and geochemical constraints on chromium oxidation induced by birnessite.
719 *Applied Geochemistry*, *108*. https://doi.org/10.1016/j.apgeochem.2019.104365
720 Kwon, K. D., Refson, K., & Sposito, G. (2010). Surface complexation of Pb(II) by hexagonal
721 birnessite nanoparticles. *Geochimica et Cosmochimica Acta*, *74*(23), 6731–6740.
722 https://doi.org/10.1016/j.gca.2010.09.002
723 Lafferty, B. J., Ginder-Vogel, M., & Sparks, D. L. (2011). Arsenite Oxidation by a Poorly-
724 Crystalline Manganese Oxide. 3. Arsenic and Manganese Desorption. *Environmental*
725 *Science & Technology*, *45*, 9218–9223. https://doi.org/10.1021/es201281u
726 Learman, D.R., Wankel, S. D., Webb, S. M., Martinez, N., Madden, A. S., & Hansel, C. M.
727 (2011). Coupled biotic–abiotic Mn(II) oxidation pathway mediates the formation and
728 structural evolution of biogenic Mn oxides. *Geochimica et Cosmochimica Acta*, *75*, 6048–
729 6063. https://doi.org/10.1016/j.gca.2011.07.026

730 Learman, Deric R, Voelker, B. M., Madden, A. S., & Hansel, C. M. (2013). Constraints on
731 superoxide mediated formation of manganese oxides. *Frontiers in Microbiology*, *4*, 1–11.
732 https://doi.org/10.3389/fmicb.2013.00262
733 Ling, F. T., Heaney, P. J., Post, J. E., & Gao, X. (2015). Transformations from triclinic to
734 hexagonal birnessite at circumneutral pH induced through pH control by common
735 biological buffers. *Chemical Geology*, *416*, 1–10.
736 https://doi.org/10.1016/j.chemgeo.2015.10.007
737 Ling, F. T., Post, J. E., Heaney, P. J., & Ilton, E. S. (2018). The relationship between Mn
738 oxidation state and structure in triclinic and hexagonal birnessites. *Chemical Geology*,
739 *479*(January), 216–227. https://doi.org/10.1016/j.chemgeo.2018.01.011
740 Lopano, C. L., Heaney, P. J., & Post, J. E. (2009). Cs-exchange in birnessite: Reaction
741 mechanisms inferred from time-resolved X-ray diffraction and transmission electron
742 microscopy. *American Mineralogist*, *94*, 816–826. https://doi.org/10.2138/am.2009.3068
743 Lopano, C. L., Heaney, P. J., Post, J. E., Hanson, J., & Komarneni, S. (2007). Time-resolved
744 structural analysis of K- and Ba-exchange reactions with synthetic Na-birnessite using
745 synchrotron X-ray diffraction. *American Mineralogist*, *92*, 380–387.
746 https://doi.org/10.2138/am.2007.2242
747 Lopano, Christina L., Heaney, P. J., Bandstra, J. Z., Post, J. E., & Brantley, S. L. (2011). Kinetic
748 analysis of cation exchange in birnessite using time-resolved synchrotron X-ray diffraction.
749 *Geochimica et Cosmochimica Acta*, *75*(14), 3973–3981.
750 https://doi.org/10.1016/j.gca.2011.04.021
751 Luan, F., Santelli, C. M., Hansel, C. M., & Burgos, W. D. (2012). Defining manganese(II)
752 removal processes in passive coal mine drainage treatment systems through laboratory

753 incubation experiments. *Applied Geochemistry*, *27*(8), 1567–1578.
754 https://doi.org/10.1016/j.apgeochem.2012.03.010
755 Manceau, A., Gorshkov, A. I., & Drits, V. A. (1992). Structural chemistry of Mn, Fe, Co, and Ni
756 in manganese hydrous oxides: Part I. Information from XANES spectroscopy. *American*
757 *Mineralogist*, *77*, 1133–1143.
758 Manceau, A., Marcus, M. A., & Tamura, N. (2002). Quantitative Speciation of Heavy Metals in
759 Soils and Sediments by Synchrotron X-ray Techniques. *Applications of Synchrotron*
760 *Radiation in Low-Temperature Geochemistry and Environmental Science*, *49*, 341–428.
761 Manceau, Alain, Lanson, M., & Geoffroy, N. (2007). Natural speciation of Ni, Zn, Ba, and As in
762 ferromanganese coatings on quartz using X-ray fluorescence, absorption, and diffraction.
763 *Geochimica et Cosmochimica Acta*, *71*, 95–128. https://doi.org/10.1016/j.gca.2006.08.036
764 Manceau, Alain, Marcus, M. A., & Grangeon, S. (2012). Determination of Mn valence states in
765 mixed-valent manganates by XANES spectroscopy. *American Mineralogist*, *97*, 816–827.
766 https://doi.org/10.2138/am.2012.3903
767 McKeown, D. A., & Post, J. E. (2001). Characterization of manganese oxide mineralogy in rock
768 varnish and dendrites using X-ray absorption spectroscopy. *American Mineralogist*, *86*,
769 701–713. Retrieved from %5C%5CScancyp%5CLiteratur%5CLit6-pdf%5CAmerMineral
770 86 McKeown_701-713_01.pdf
771 Murray, J. W., & Dillard, J. G. (1979). The oxidation of cobalt(II) adsorbed on manganese
772 dioxide. *Geochimica et Cosmochimica Acta*, *43*, 781–787.
773 Oscarson, D. W., Huang, P. M., Defosse, C., & Herbillon, A. (1981). Oxidative power of
774 Mn(IV) and Fe(III) oxides with respect to As(III) in terrestrial and aquatic environments.
775 *Nature*, *291*, 50–51.

776 Paterson, E., Bunch, J. L., & Clark, D. R. (1986). Cation exchange in synthetic manganates: I.
777 Alkylammonium exchange in a synthetic phyllomanganate. *Clay Minerals*, *21*, 949–955.
778 Peacock, C. L., & Moon, E. M. (2012). Oxidative scavenging of thallium by birnessite:
779 Explanation for thallium enrichment and stable isotope fractionation in marine
780 ferromanganese precipitates. *Geochimica et Cosmochimica Acta*, *84*, 297–313.
781 https://doi.org/10.1016/j.gca.2012.01.036
782 Post, J.E. (1999). Manganese oxide minerals: Crystal structures and economic and environmental
783 significance. *Proceedings of the National Academy of Sciences*, *96*, 3447–3454.
784 https://doi.org/10.1073/pnas.96.7.3447
785 Post, J.E., Heaney, P. J., & Ertl, A. (2008). Rietveld refinement of the ranciéite structure using
786 synchrotron powder diffraction data. *Powder Diffraction*, *23*(1), 10–14.
787 https://doi.org/10.1154/1.2836477
788 Post, J.E., Heaney, P. J., & Hanson, J. (2002). Rietveld refinement of a triclinic structure for
789 synthetic Na-birnessite using synchrotron powder diffraction. *Powder Diffraction*, *17*(3),
790 218–221.
791 Post, J.E., & Veblen, D. R. (1990). Crystal structure determinations of synthetic sodium,
792 magnesium, and postassium birnessite using TEM and the Rietveld Method. *American*
793 *Mineralogist*, *75*, 477–489.
794 Post, Jeffrey E., Heaney, P. J., & Ertl, A. (2008). Rietveld refinement of the ranciéite structure
795 using synchrotron powder diffraction data. *Powder Diffraction*, *23*, 10–14.
796 https://doi.org/10.1154/1.2836477
797 Potter, R. M., & Rossman, G. R. (1979). The tetravalent manganese oxides : identification ,
798 hydration , and structural relationships by infrared spectroscopy. *American Mineralogist*,

799 *64*, 1199–1218. Retrieved from
800 http://www.minsocam.org/ammin/AM64/AM64_1199.pdf?ref=PandoraISP
801 Ravel, B., & Newville, M. (2005). ATHENA , ARTEMIS , HEPHAESTUS : data analysis for X-
802 ray absorption spectroscopy using IFEFFIT. *Journal of Synchrotron Radiation*, *12*, 537–
803 541. https://doi.org/10.1107/S0909049505012719
804 Remucal, C. K., & Ginder-Vogel, M. (2014). A critical review of the reactivity of manganese
805 oxides with organic contaminants. *Environmental Sciences: Processes and Impacts*, *16*(6),
806 1247–1266. https://doi.org/10.1039/c3em00703k
807 Richmond, W. E., Fleischer, M., & Mrose, M. E. (1969). Studies on manganese oxide minerals.
808 IX. Rancieite. *Bulletin de La Societe Francaise Mineralogie et de Cristallographie*, *92*(2),
809 191–195.
810 Santelli, C. M., Pfister, D. H., Lazarus, D., Sun, L., Burgos, W. D., & Hansel, C. M. (2010).
811 Promotion of Mn(II) oxidation and remediation of coal mine drainage in passive treatment
812 systems by diverse fungal and bacterial communities. *Applied and Environmental*
813 *Microbiology*, *76*(14), 4871–4875. https://doi.org/10.1128/AEM.03029-09
814 Santelli, C. M., Webb, S. M., Dohnalkova, A. C., & Hansel, C. M. (2011). Diversity of Mn
815 oxides produced by Mn(II)-oxidizing fungi. *Geochimica et Cosmochimica Acta*, *75*, 2762–
816 2776. https://doi.org/10.1016/j.gca.2011.02.022
817 Saratovsky, I., Gurr, S. J., & Hayward, M. A. (2009). The Structure of manganese oxide formed
818 by the fungus Acremonium sp. strain KR21-2. *Geochimica et Cosmochimica Acta*, *73*,
819 3291–3300. https://doi.org/10.1016/j.gca.2009.03.005
820 Saratovsky, I., Wightman, P. G., Pastén, P. A., Gaillard, J.-F., & Poeppelmeier, K. R. (2006).
821 Manganese Oxides: Parallels between Abiotic and Biotic Structures. *Journal of the*

822 *American Chemical Society*, *128*, 11188–11198. https://doi.org/10.1021/ja062097g
823 Sayers, D. E., & Bunkers, B. A. (1988). *X-ray Absorption Principles, Applications, Techniques*
824 *of EXAFS, SEXAFS, and XANES*. New York: Wiley.
825 Scott, J. M., & Morgan, J. J. (1996). Reactions at oxide surfaces. 2. Oxidation of Se(IV) by
826 synthetic Birnessite. *Environmental Science & Technology*, *30*, 1990–1996.
827 https://doi.org/10.1021/es950741d
828 Silvester, E., Manceau, A., & Drits, V. A. (1997). Structure of synthetic monoclinic Na-rich
829 birnessite and hexagonal birnessite: II. Results from chemical studies and EXAFS
830 spectroscopy. *American Mineralogist*, *82*, 962–978.
831 Simanova, A. A., Kwon, K. D., Bone, S. E., Bargar, J. R., Refson, K., Sposito, G., & Peña, J.
832 (2015). Probing the sorption reactivity of the edge surfaces in birnessite nanoparticles using
833 nickel(II). *Geochimica et Cosmochimica Acta*, 191–204.
834 https://doi.org/10.1016/j.gca.2015.04.050
835 Simanova, A. a., & Peña, J. (2015). Time-resolved investigation of cobalt oxidation by Mn(III)-
836 rich δ-MnO2 using quick X-ray absorption spectroscopy. *Environmental Science &*
837 *Technology*, *49*, 10867–10876. https://doi.org/10.1021/acs.est.5b01088
838 Sommers, M. G., Dollhopf, M. E., & Douglas, S. (2002). Freshwater ferromanganese
839 stromatolites from Lake Vermilion, Minnesota: Microbial culturing and environmental
840 scanning electron microscopy investigations. *Geomicrobiology Journal*, *19*(4), 407–427.
841 Retrieved from isi:000177532300002
842 Stuckey, J. W., Goodwin, C., Wang, J., Kaplan, L. A., Vidal-Esquivel, P., Beebe, T. P., &
843 Sparks, D. L. (2018). Impacts of hydrous manganese oxide on the retention and lability of
844 dissolved organic matter. *Geochemical Transactions*, *19*, 1–19.

https://doi.org/10.1186/s12932-018-0051-x

Tan, H., Zhang, G., Heaney, P. J., Webb, S. M., & Burgos, W. D. (2010). Characterization of manganese oxide precipitates from Appalachian coal mine drainage treatment systems. *Applied Geochemistry*, *25*, 389–399. https://doi.org/10.1016/j.apgeochem.2009.12.006

Toner, B., Manceau, A., Webb, S. M., & Sposito, G. (2006). Zinc sorption to biogenic hexagonal-birnessite particles within a hydrated bacterial biofilm. *Geochimica et Cosmochimica Acta*, *70*, 27–43. https://doi.org/10.1016/j.gca.2005.08.029

Usui, A., & Mita, N. (1994). IX. Mineralogy, geochemistry and internal growth structure of manganese nodules in the western part of the Penrhyn Basin, South Pacific (GH83-3 area). *Geological Survey of Japan Cruise Report*, (23), 165–185.

Villalobos, M., Lanson, B., Manceau, A., Toner, B., & Sposito, G. (2006). Structural model for the biogenic Mn oxide produced by Pseudomonas putida. *American Mineralogist*, *91*, 489–502. https://doi.org/10.2138/am.2006.1925

Villalobos, Mario, Toner, B., Bargar, J., & Sposito, G. (2003). Characterization of the manganese oxide produced by Pseudomonas putida strain MnB1. *Geochimica et Cosmochimica Acta*, *67*(14), 2649–2662. https://doi.org/10.1016/S0016-7037(03)00217-5

Weaver, R. M., & Hochella, M. F. J. (2003). The reactivity of seven Mn-oxides with Cr 3 + aq : A comparative analysis of a complex , environmentally important redox reaction. *American Mineralogist*, *88*, 2016–2027.

Webb, S. M., Tebo, B. M., & Barger, J. R. (2005). Structural Influences of Sodium and Calcium Ions on the Biogenic Manganese Oxides Produced by the Marine Bacillus Sp., Strain SG-1. *Geomicrobiology Journal*, *22*, 181–193. https://doi.org/10.1080/01490450590946013

Webb, S.M., Tebo, B. M., & Bargar, J. R. (2005). Structural characterization of biogenic Mn

868 oxides produced in seawater by the marine bacillus sp. strain SG-1. *American Mineralogist*,
869 *90*, 1342–1357. https://doi.org/10.2138/am.2005.1669
870 Webb, Sam M., Tebo, B. M., & Bargar, J. R. (2005a). Structural characterization of biogenic Mn
871 oxides produced in seawater by the marine bacillus sp. strain SG-1. *American Mineralogist*,
872 *90*, 1342–1357. https://doi.org/10.2138/am.2005.1669
873 Webb, Sam M., Tebo, B. M., & Bargar, J. R. (2005b). Structural characterization of biogenic Mn
874 oxides produced in seawater by the marine bacillus sp. strain SG-1. *American Mineralogist*,
875 *90*(8–9), 1342–1357. https://doi.org/10.2138/am.2005.1669
876 Zhao, H., Zhu, M., Li, W., Elzinga, E. J., Villalobos, M., Liu, F., … Sparks, D. L. (2016). Redox
877 Reactions between Mn(II) and Hexagonal Birnessite Change its Layer Symmetry.
878 *Environmental Science & Technology*, 1–33. https://doi.org/10.1021/acs.est.5b04436
879 Zhao, W., Liu, F., Feng, X., Tan, W., Qiu, G., & Chen, X. (2012). Fourier transform infrared
880 spectroscopy study of acid birnessites before and after Pb2+ adsorption. *Clay Minerals*, *47*,
881 191–204. https://doi.org/10.1180/claymin.2012.047.2.04
882
883
884

FIGURE CAPTIONS

Fig. 1. Schematic diagram of (a) triclinic and (b) hexagonal birnessite after Lanson et al. (2000).

Fig. 2. XRD patterns for (a) synthetic triclinic Na-birnessite, (b) synthetic hexagonal H-birnessite, (c) France 128319, (d) rancieite Spain, and (3) Paxton Cave. These natural samples from France, Spain, and Paxton Cave were identified as hexagonal birnessite using XRD.

Fig. 3. Select SEM images of XRD-identified hexagonal birnessite samples for (a) rancieite Spain, (b) France 128319, and (c) Paxton Cave.

Fig. 4. XRD patterns for (a) synthetic triclinic Na-birnessite, (b) synthetic hexagonal H-birnessite, (c) the fungally precipitated 3-line birnessite fungal Stag50Ca1.6Mn, and natural 3-line birnessite samples (d) Glasgow, (e) Vermilion, (f) DS1-M3f, (g) DS2-M3f, (h) PBS-M2f-1, (i) PBS-M2f-2, and (j) Spring Branch. The dotted lines represent the identifying d-spacings for 3-line birnessite.

Fig. 5. Select SEM images of 3-line birnessite samples (a) DS1-M3f, (b) Glasgow, (c) DS2-M3f, (d) Spring Branch, (e) PBS-M2f-1, and (f) Vermilion.

Fig. 6. $\chi(k)$ plots of 3-line birnessite samples with overlays of synthetic triclinic Na-birnessite and synthetic hexagonal H-birnessite $\chi(k)$ plots.

Fig. 7. Radial distribution functions (RDFs) of 3-line birnessite samples with overlays of synthetic triclinic Na-birnessite and synthetic hexagonal H-birnessite RDFs.

Fig. 8. $\chi(k)$ plots of XRD-identified hexagonal birnessite samples with overlays of synthetic triclinic Na-birnessite and synthetic hexagonal H-birnessite $\chi(k)$ plots.

Fig. 9. Radial distribution functions (RDFs) of XRD-identified hexagonal birnessite with overlays of synthetic triclinic Na-birnessite and synthetic hexagonal H-birnessite RDFs.

908 **Fig. 10**. Mn oxidation state ratios determined from XPS for select samples Paxton Cave,
909 Glasgow, and Spring Branch compared to synthetic triclinic and synthetic hexagonal
910 birnessites.
911 **Fig. 11**. FTIR spectra of (a) synthetic triclinic Na-birnessite, and XRD-identified hexagonal (b)
912 Paxton Cave, (c) rancieite Spain, (d) France 128319 samples, and (d) synthetic hexagonal
913 H-birnessite.
914 **Fig. 12**. FTIR spectra of (a) synthetic triclinic Na-birnessite, the 3-line birnessites (b) Spring
915 Branch, (c) PBS-M2f-1, (d) PBS-M2f-2, (e) DS2-M3f, (f) Vermilion, (g) DS1-M3f, (h)
916 Glasgow, (i) fungal Stag50Ca1.5Mn, and (j) synthetic hexagonal H-birnessite.
917 **Fig. 13**. FTIR spectra of original buserites and their spectra after drying at 110°C to become
918 birnessite for (a-b) Spring Branch, (c-d) PBS-M2f-1, (e-f) PBS-M2f-2, (g-h) DS2-M3f,
919 (i-j) DS1-M3f.
920 **Fig. 14**. (a) Trends in Peak 1, Peak 2, and Peak 3 observed from the FTIR for 3-line birnessites
921 as hexagonality increases according to LCF of EXAFS data. (b) The peak shifts are
922 depicted in the FTIR spectra in the range from 400 to 650 cm^{-1}.
923 **Fig. 15**. Trends in Peak 1, Peak 2, and Peak 3 observed from FTIR according to their Mn^{3+}
924 concentrations for the select samples on which XPS was conducted. Samples include
925 synthetic hexagonal birnessite (HB), synthetic triclinic Na-birnessite (NaB), Paxton Cave
926 (PC), Glasgow (GL), and Spring Branch (SB).

This is a preprint, the final version is subject to change, of the American Mineralogist (MSA)
Cite as Authors (Year) Title. American Mineralogist, in press.
DOI: https://doi.org/10.2138/am-2020-7303

927 **TABLES**

928

929 **Table 1**. List of birnessite samples, categorized as either XRD-identified hexagonal birnessites of 3-line birnessites.

Samples	**Locality**	**Chemical Formula** (calculated assuming all Mn^{4+} cations and no H^{+})	**Identified Phases**
		XRD-Identified Hexagonal Birnessites	
Paxton Cave	Paxton Cave, VA	*$(Na_{0.02}Mg_{0.06}Ca_{0.17}K_{0.03})$ $(Mn(IV)_{1.44}Mn(III)_{0.17}Mn(II)_{0.16}$ $Si_{0.09}Al_{0.07}Fe_{0.06}\square_{0.02})O_4 \bullet xH_2O$	Hexagonal birnessite˜°, diatoms (or quartz?)°×, quartz˜, calcite˜, todorokite˜
France 128319	French Pyrenees hydrothermal vein	$(Mg_{0.10}Ca_{0.24}Ba_{0.01}Zn_{0.12})$ $Mn_{1.75}\square_{0.25}O_4 \bullet xH_2O$	Hexagonal birnessite˜°, todorokite, quartz×
Spain Rancieite	Las Alpujarras, Granada, Spain	$(Mg_{0.12}Cu_{0.01}Ca_{0.23}Ba_{0.06})$ $Mn(IV)_{1.75}Cu_{0.01}Fe_{0.04}\square_{0.20}O_4 \bullet xH_2O$	Hexagonal birnessite˜°, todorokite, goethite×
		3-line Birnessites	
Glasgow	coal mine drainage treatment site in Glasgow, PA	*$(Na_{0.01}Mg_{0.02}Ca_{0.04}K_{0.01}Mn(II)_{0.34}Mn(III)_{0.06})$ $(Mn(IV)_{1.32}Mn(III)_{0.40}\square_{0.13}Si_{0.03}Fe_{0.13})O_4 \bullet xH_2O$	birnessite˜°, calcite/dolomite˜°, diatoms×°
DS1-M3f	coal mine drainage treatment site in De Sale, PA	$(Mg_{0.049}Ca_{0.163}K_{0.028})$ $Mn(IV)_{1.70}Si_{0.09}Al_{0.07}Fe_{0.05}\square_{0.11}O4 \bullet xH_2O$	buserite˜°, calcite?°, diatoms×°, aluminosilicates×°
DS2-M3f	coal mine drainage treatment site in De Sale, PA	$(Na_{0.05}Mg_{0.06}Ca_{0.10}K_{0.03}Zn_{0.01})$ $Mn(IV)_{1.36}Si_{0.10}Al_{0.33}Fe_{0.19}\square_{0.02}O_4 \bullet xH_2O$	buserite˜°, calcite?°, quartz˜°, diatoms×°, aluminosilicates×°
PBS-M2f-1	coal mine drainage treatment site near Central City, PA	$(Na_{0.02}Mg_{0.05}Ca_{0.09}Zn_{0.03})$ $Mn(IV)_{1.60}Si_{0.02}Al_{0.31}Fe_{0.04}\square_{0.03}O_4 \bullet xH_2O$	buserite˜°, quartz˜°, calcite/dolomite˜°, aluminosilicates×°

PBS-M2f-2	coal mine drainage treatment site, sampled at a different time than PBS-M2f-1	N/A	buserite˜°, quartz˜°, calcite/dolomite˜°, aluminosilicates° (no SEM done)
Vermilion	lake nodule from Lake Vermilion, MI	$(Mg_{0.01}Ca_{0.04}K_{0.02}Ba_{0.16})$ $Mn(IV)_{1.85}Si_{0.01}Al_{0.02}Fe_{0.01}\square_{0.12}O_4 \bullet xH_2O$	birnessite˜°, goethite˜, aluminosilicates×°, calcite/dolomite?°
Spring Branch	Spring Branch, TN	$*(Mg_{0.06}Ca_{0.28}K_{0.01})$ $(Mn(IV)_{0.94}Mn(III)_{0.88}Mn(II)_{0.05}Si_{0.03}Al_{0.01}Fe_{0.04}\square_{0.13})O_4 \bullet xH_2O$	birnessite˜°, calcite/dolomite˜°, diatoms×°, aluminosilicates×°
Fungal Stag50Ca1.5Mn	bioprecipitated by *Stagnospora sp*. SRC11sM3a	N/A	birnessite˜°, fungi°

Cations below the analytical threshold were not included in the chemical formulas.
*chemical formulas calculated with Mn oxidation states determined from XPS
˜observed in XRD
°observed in FTIR
×phase observed in SEM

This is a preprint, the final version is subject to change, of the American Mineralogist (MSA)
Cite as Authors (Year) Title. American Mineralogist, in press.
DOI: https://doi.org/10.2138/am-2020-7303

937 **Table 2**. EXAFS linear combination fitting results.

EXAFS Linear Combination Fitting				
Well-crystalline	*Vol. fraction triclinic Na-birnessite*	*Vol. fraction pH 2 hexagonal birnessite*	*Vol. fraction todorokite*	*R-factor*
France 128319	0.19 ± 0.05	0.52 ± 0.05	0.29 ± 0.06	0.0569
Rancieite Spain	0.19 ± 0.06	0.56 ± 0.04	0.26 ± 0.06	0.0440
Paxton Cave	0.15 ± 0.04	0.69 ±0.04	0.16 ± 0.05	0.0370
Poorly-crystalline				
CaBuserite TN	0.56 ± 0.02	0.44 ± 0.03	N/A	0.0230
DS2-M3f	0.46 ± 0.03	0.54 ±0.04	N/A	0.0376
PBS-M2f-1	0.43 ± 0.05	0.58 ± 0.06	N/A	0.1000
PBS-M2f-2	0.43 ± 0.03	0.57 ± 0.03	N/A	0.0317
Vermilion	0.32 ± 0.03	0.68 ± 0.03	N/A	0.0334
Glasgow MRU3P1	0.24 ± 0.03	0.76 ± 0.03	N/A	0.0550
DS1-M3f	0.22 ± 0.03	0.78 ± 0.04	N/A	0.0494
Stag50Ca1.5Mn	0.07 ± 0.04	0.93 ± 0.05	N/A	0.0991

938
939

This is a preprint, the final version is subject to change, of the American Mineralogist (MSA)
Cite as Authors (Year) Title. American Mineralogist, in press.
DOI: https://doi.org/10.2138/am-2020-7303

940 **Table 3**. FTIR peaks for birnessites.

Sample	Peak 1	Peak 2	Peak 3
XRD-identified hexagonal			
Paxton Cave	426	(456)[q]	492
Spain Rancieite	430		494
France 128319	430		495
Synthetic			
Synthetic hexagonal H-birnessite	(435)[b]	447	496
Synthetic triclinic Na-birnessite	418	478	511
3-line			
Spring Branch	425	473	514
DS2-M3f	432	471	514
PBS-M2f-1	433	472	517
PBS-M2f-2	432	471	512
Vermilion	(429)[b]	470	503
DS1-M3f	(431)[b]	468	498
Glasgow	(438)[b]	458	499
Fungal	439	(462)[b,f]	496

941 q = quartz peak
942 b = broad, subtle peak that has mostly merged into its neighboring peak
943 f = peak from fungal organic material
944
945

946

This is a preprint, the final version is subject to change, of the American Mineralogist (MSA)
Cite as Authors (Year) Title. American Mineralogist, in press.
DOI: https://doi.org/10.2138/am-2020-7303

Revision 1

FIGURES

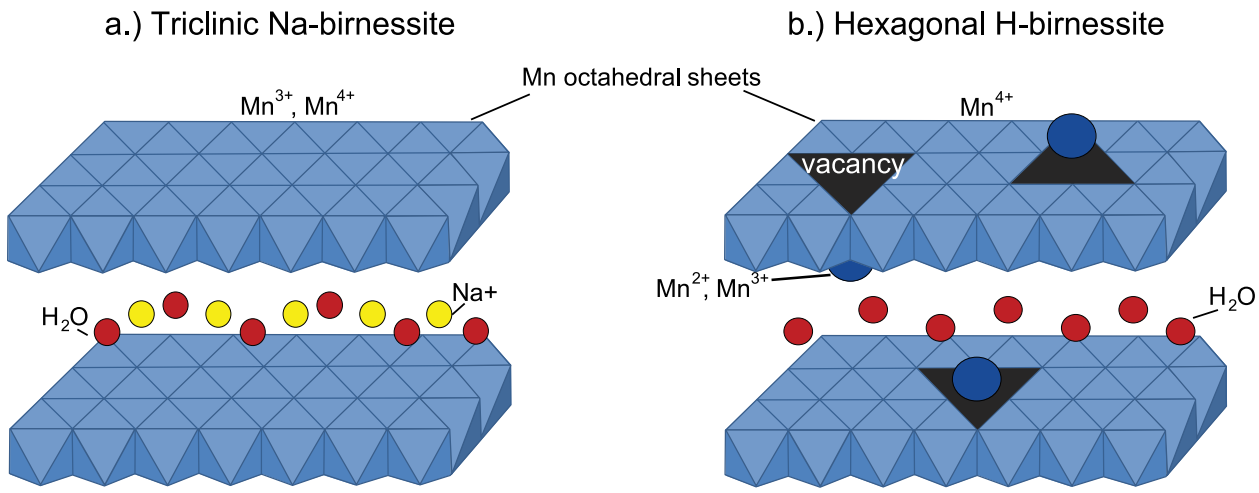

Fig. 1

This is a preprint, the final version is subject to change, of the American Mineralogist (MSA)
Cite as Authors (Year) Title. American Mineralogist, in press.
DOI: https://doi.org/10.2138/am-2020-7303

Revision 1

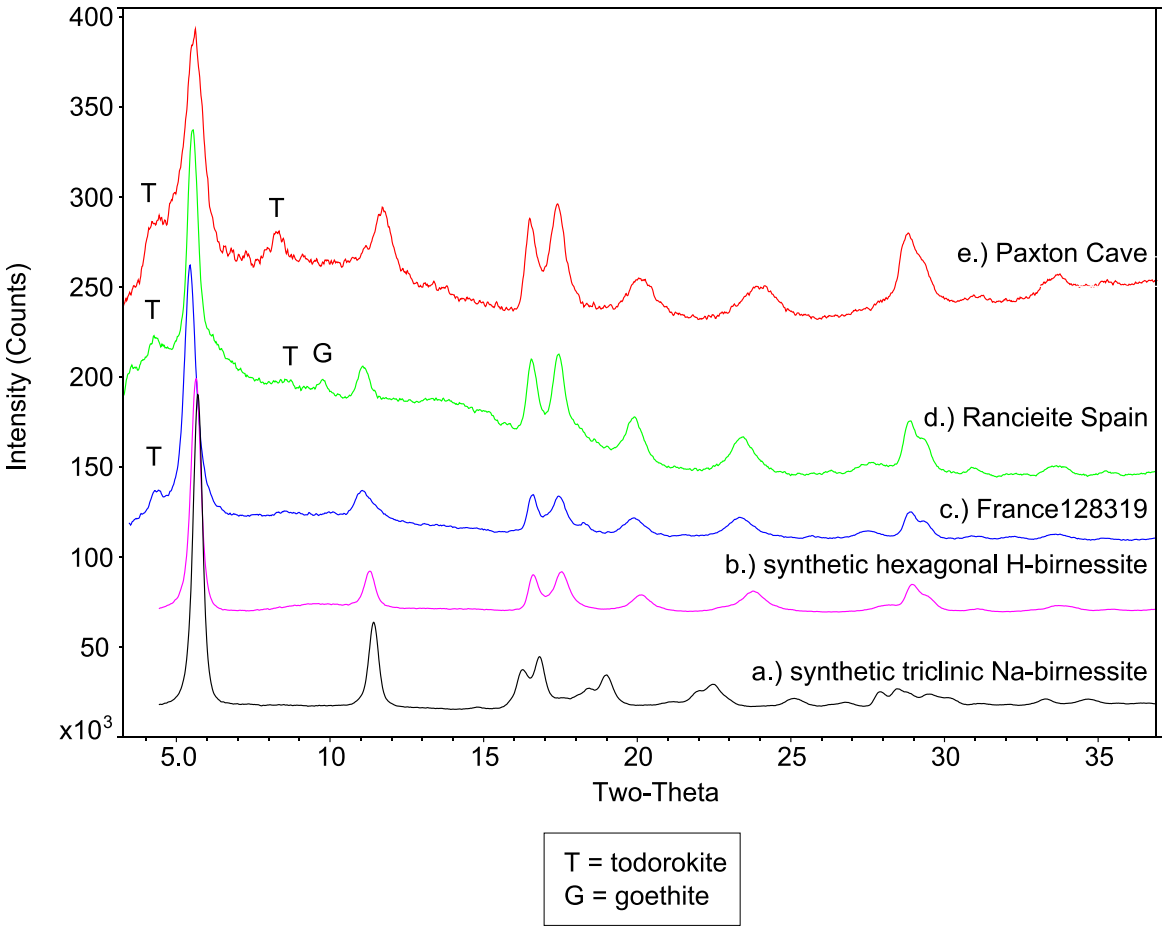

Fig. 2

This is a preprint, the final version is subject to change, of the American Mineralogist (MSA)
Cite as Authors (Year) Title. American Mineralogist, in press.
DOI: https://doi.org/10.2138/am-2020-7303

Revision 1

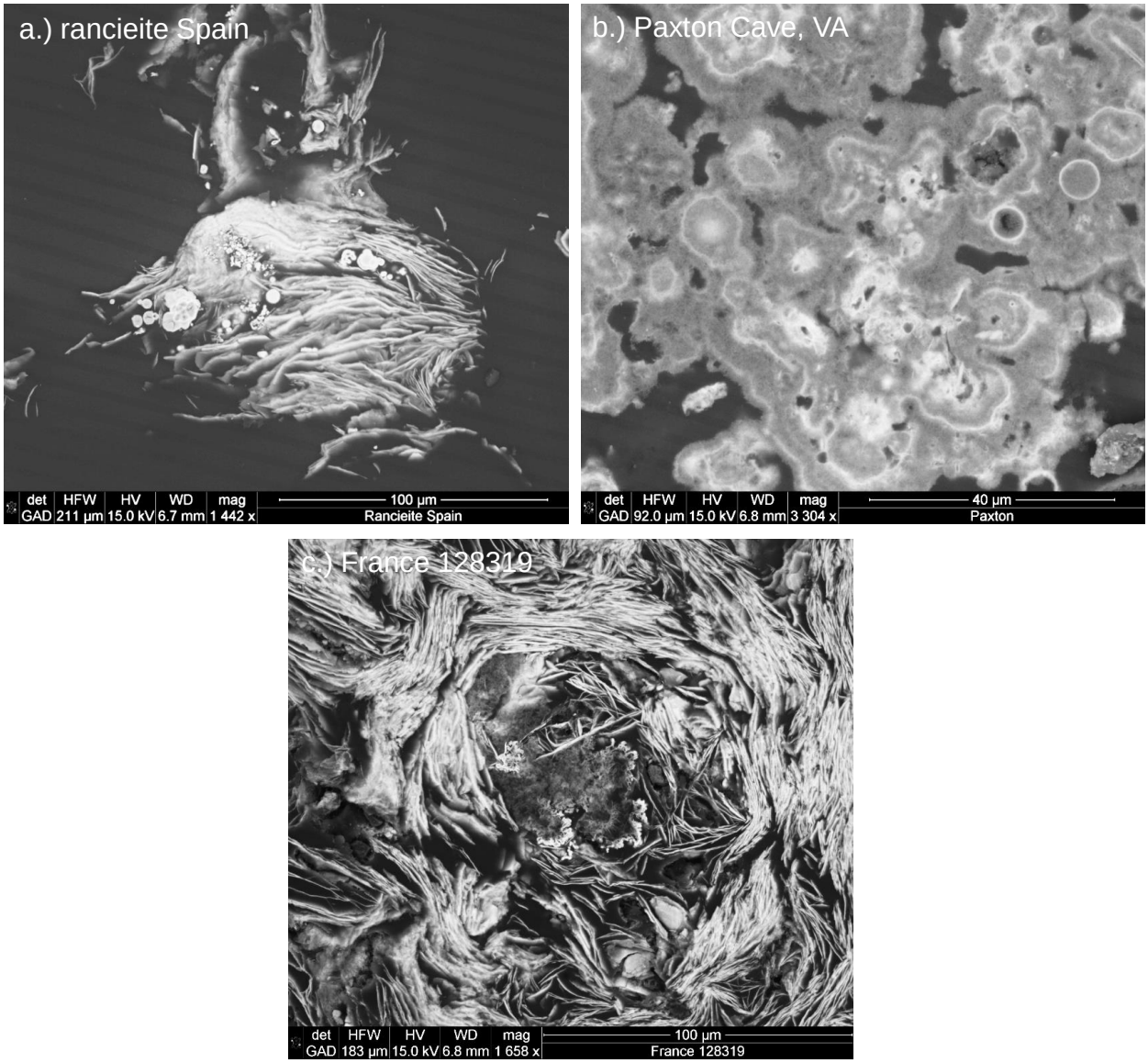

Fig. 3

This is a preprint, the final version is subject to change, of the American Mineralogist (MSA)
Cite as Authors (Year) Title. American Mineralogist, in press.
DOI: https://doi.org/10.2138/am-2020-7303

Revision 1

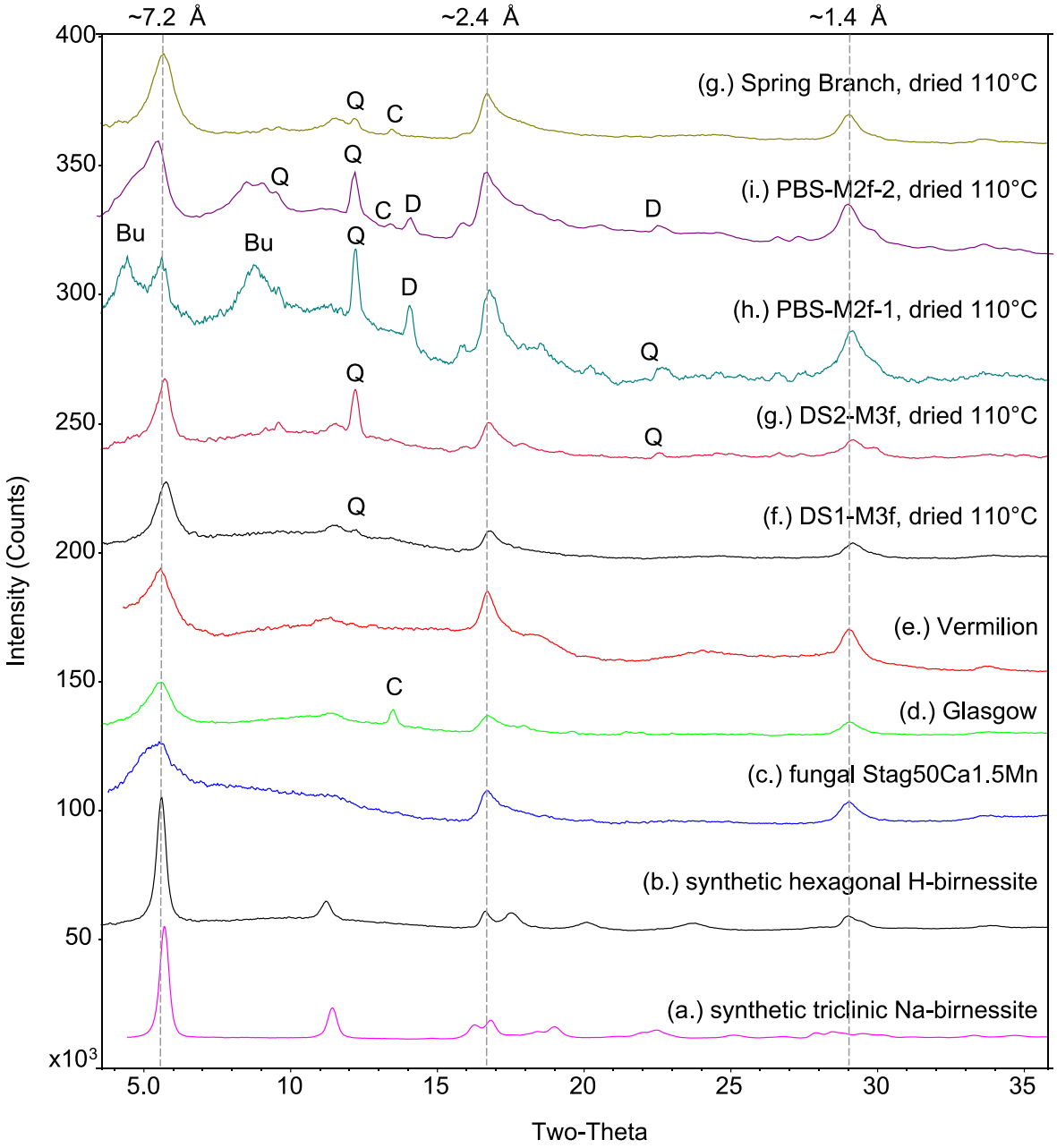

Fig. 4

This is a preprint, the final version is subject to change, of the American Mineralogist (MSA)
Cite as Authors (Year) Title. American Mineralogist, in press.
DOI: https://doi.org/10.2138/am-2020-7303

Revision 1

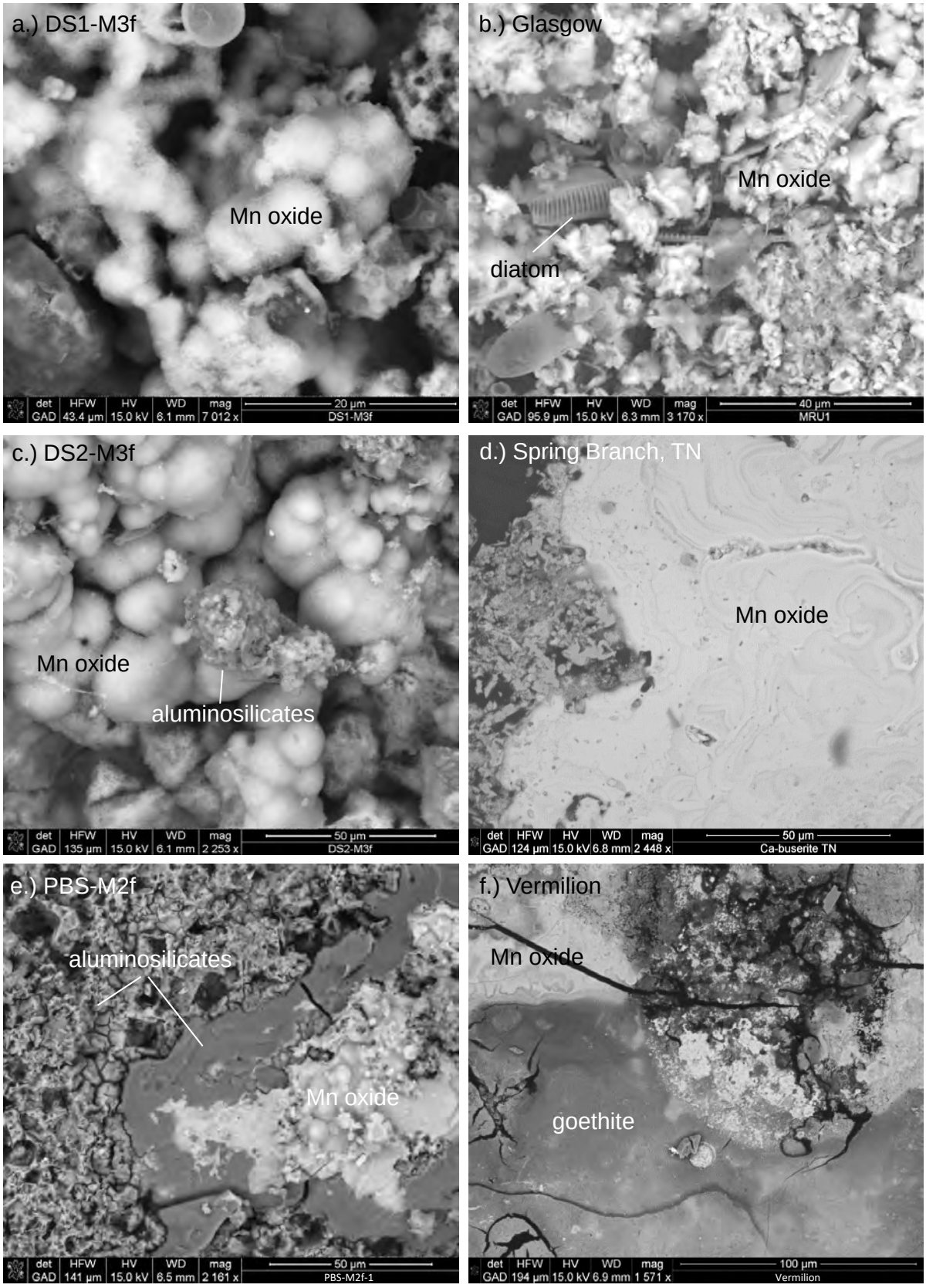

Fig. 5

This is a preprint, the final version is subject to change, of the American Mineralogist (MSA)
Cite as Authors (Year) Title. American Mineralogist, in press.
DOI: https://doi.org/10.2138/am-2020-7303

Revision 1

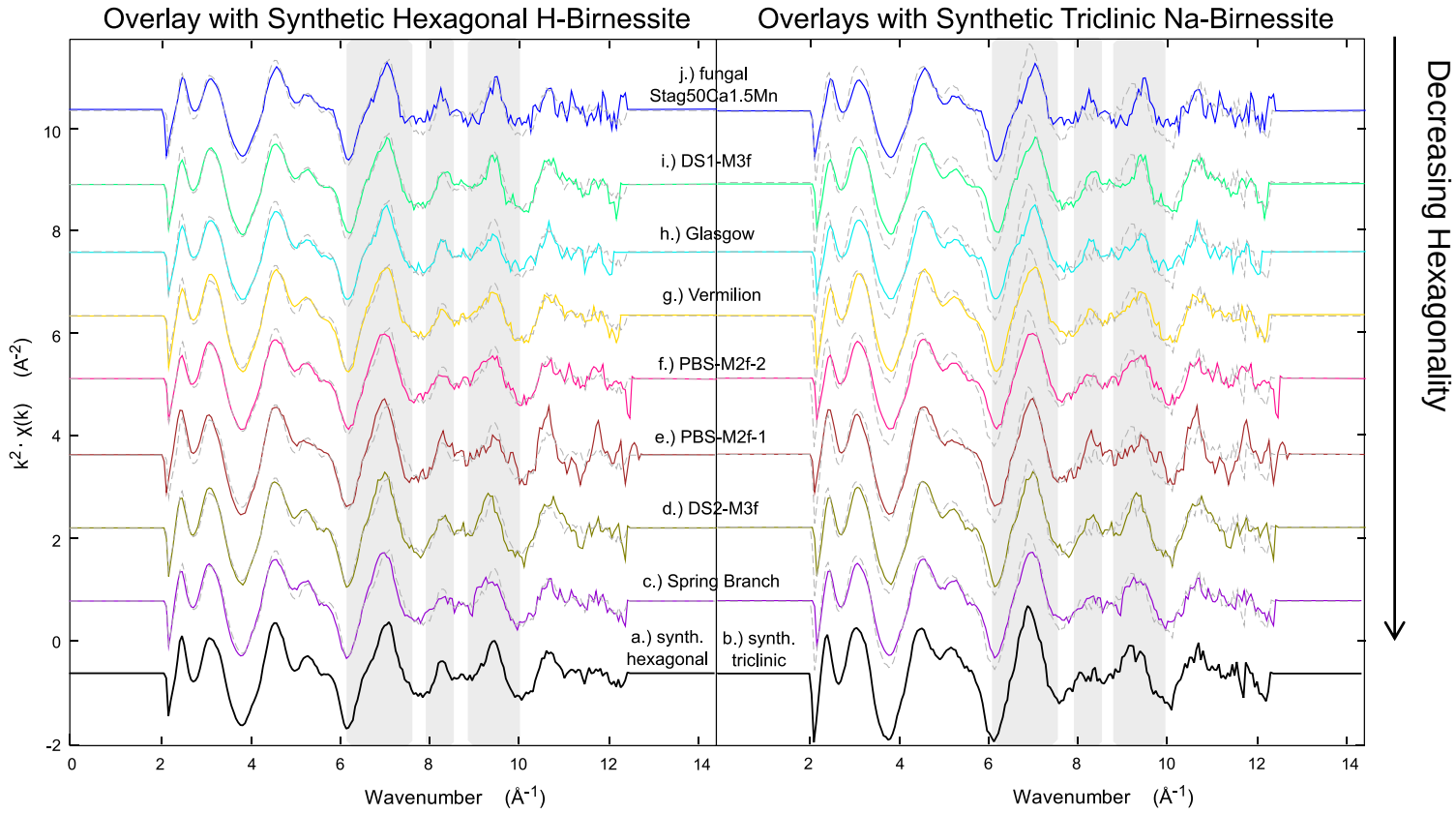

Fig. 6

This is a preprint, the final version is subject to change, of the American Mineralogist (MSA)
Cite as Authors (Year) Title. American Mineralogist, in press.
DOI: https://doi.org/10.2138/am-2020-7303

Revision 1

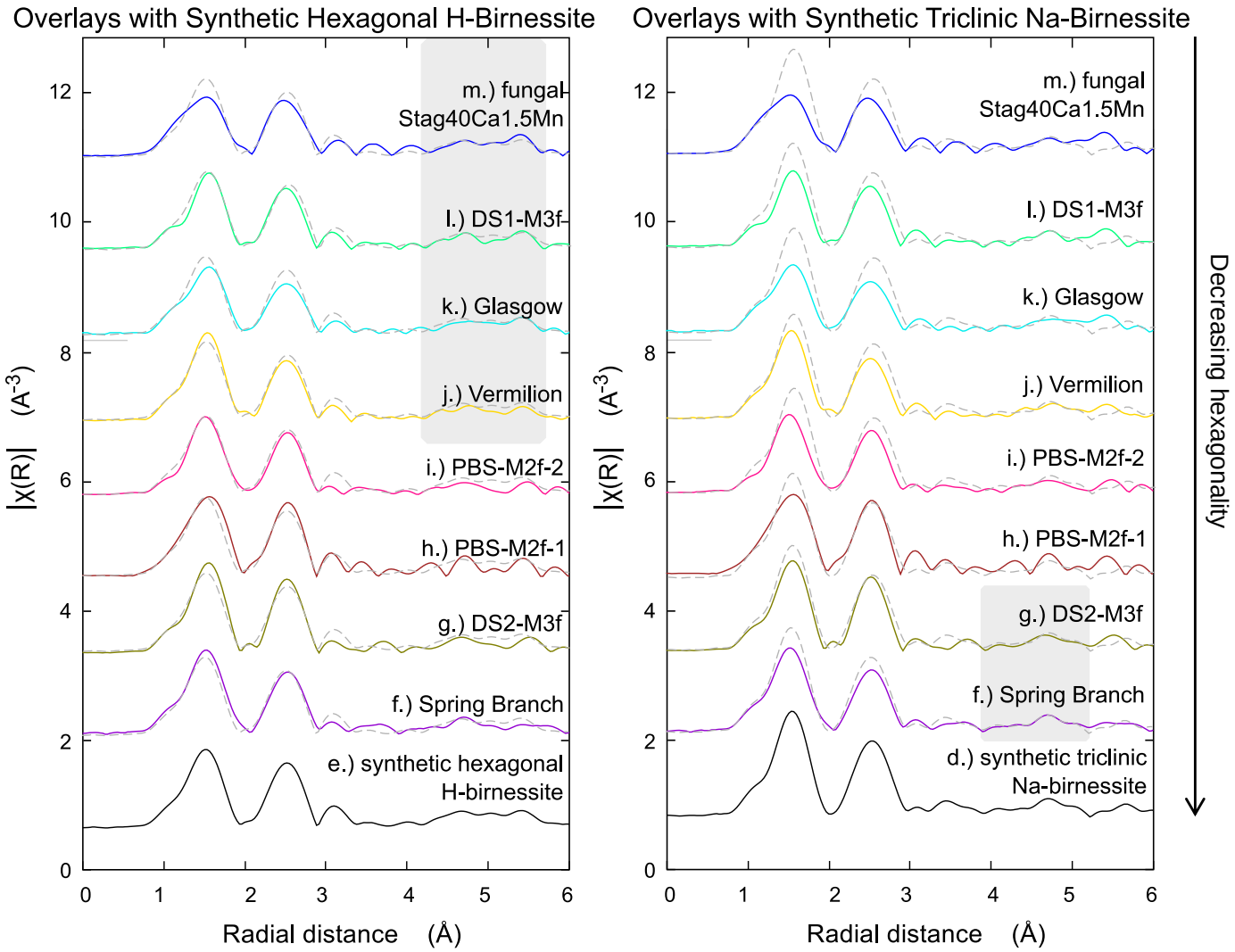

Fig. 7

This is a preprint, the final version is subject to change, of the American Mineralogist (MSA)
Cite as Authors (Year) Title. American Mineralogist, in press.
DOI: https://doi.org/10.2138/am-2020-7303

Revision 1

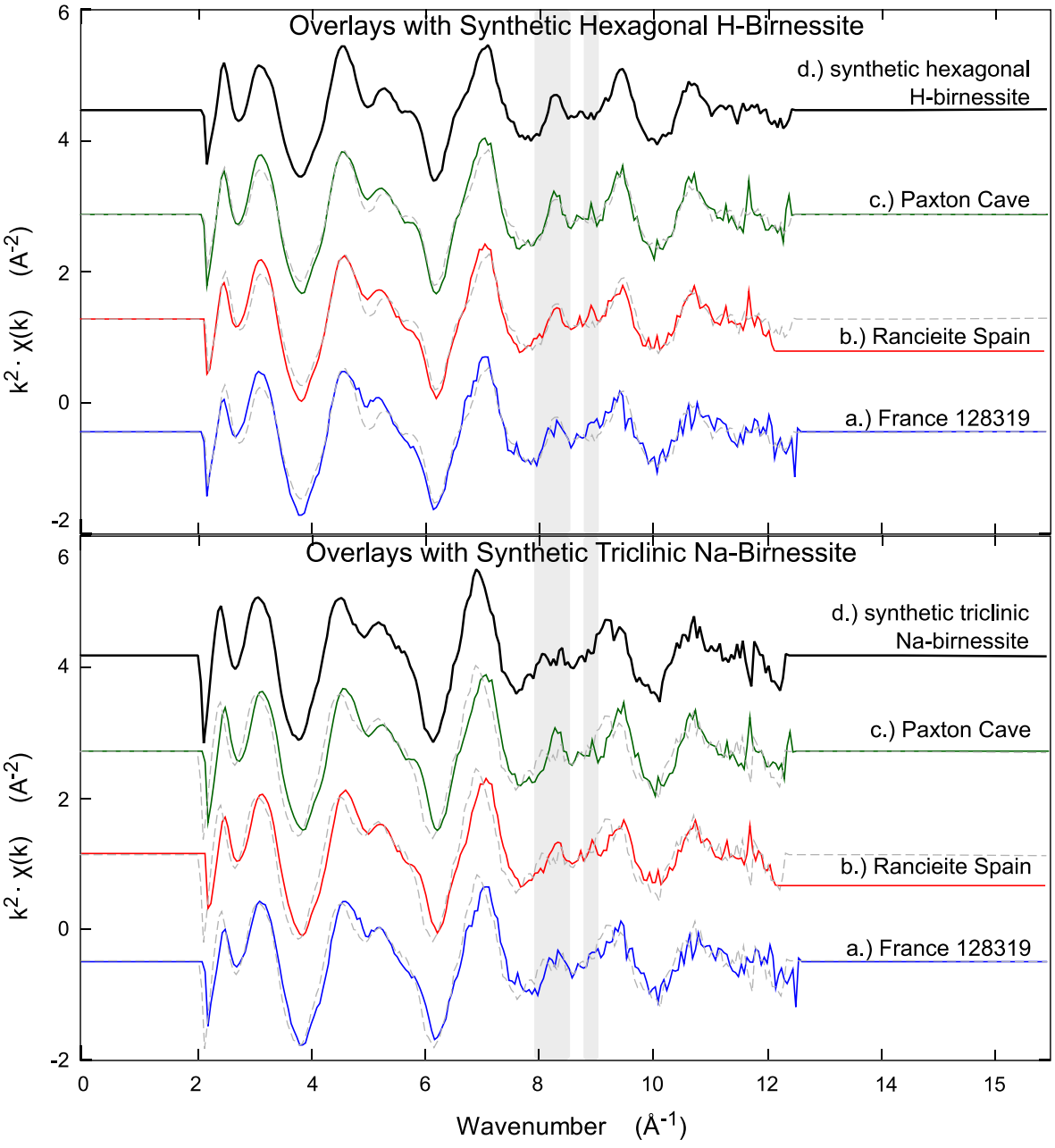

Fig. 8

This is a preprint, the final version is subject to change, of the American Mineralogist (MSA)
Cite as Authors (Year) Title. American Mineralogist, in press.
DOI: https://doi.org/10.2138/am-2020-7303

Revision 1

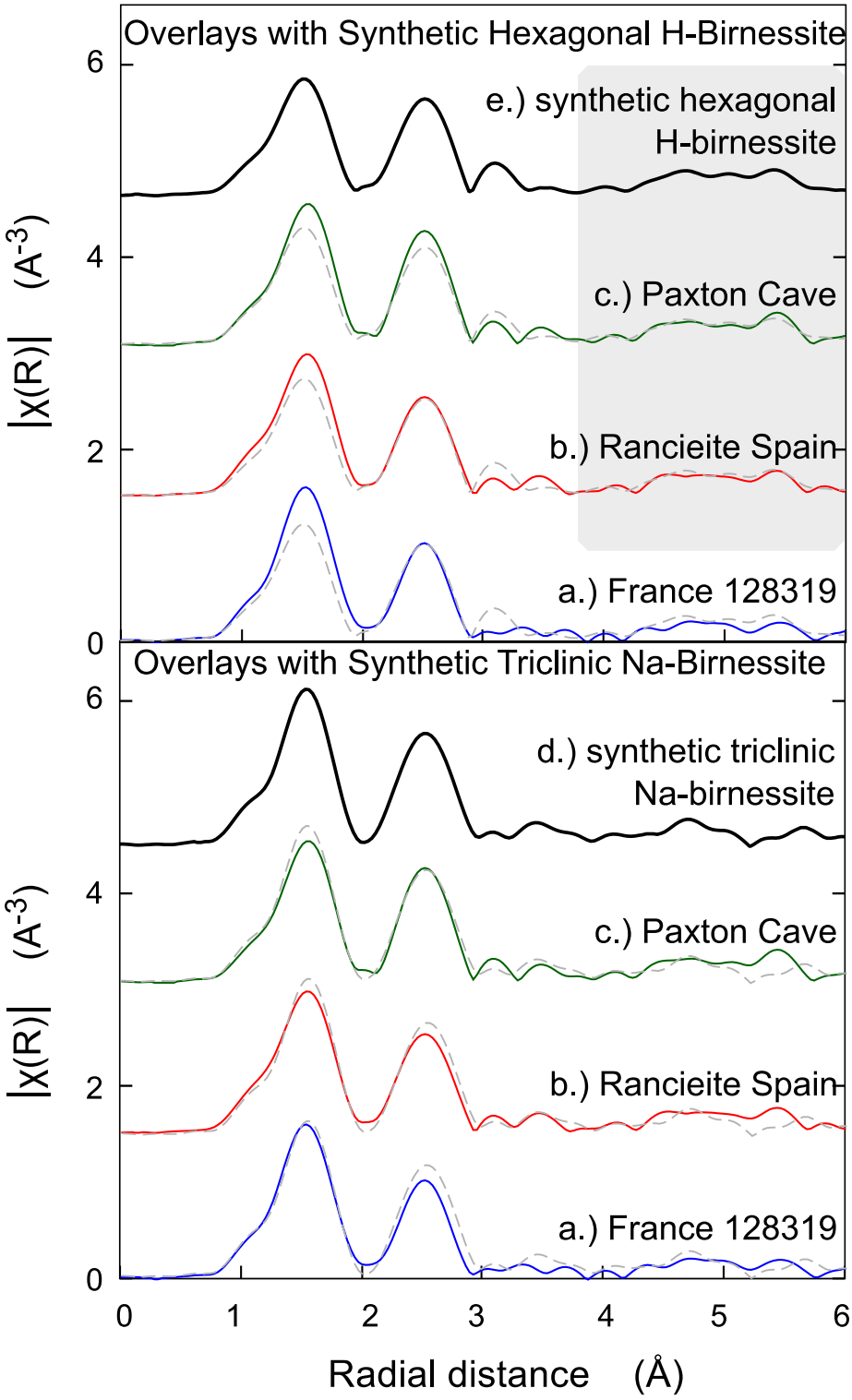

Fig. 9

This is a preprint, the final version is subject to change, of the American Mineralogist (MSA)
Cite as Authors (Year) Title. American Mineralogist, in press.
DOI: https://doi.org/10.2138/am-2020-7303

Revision 1

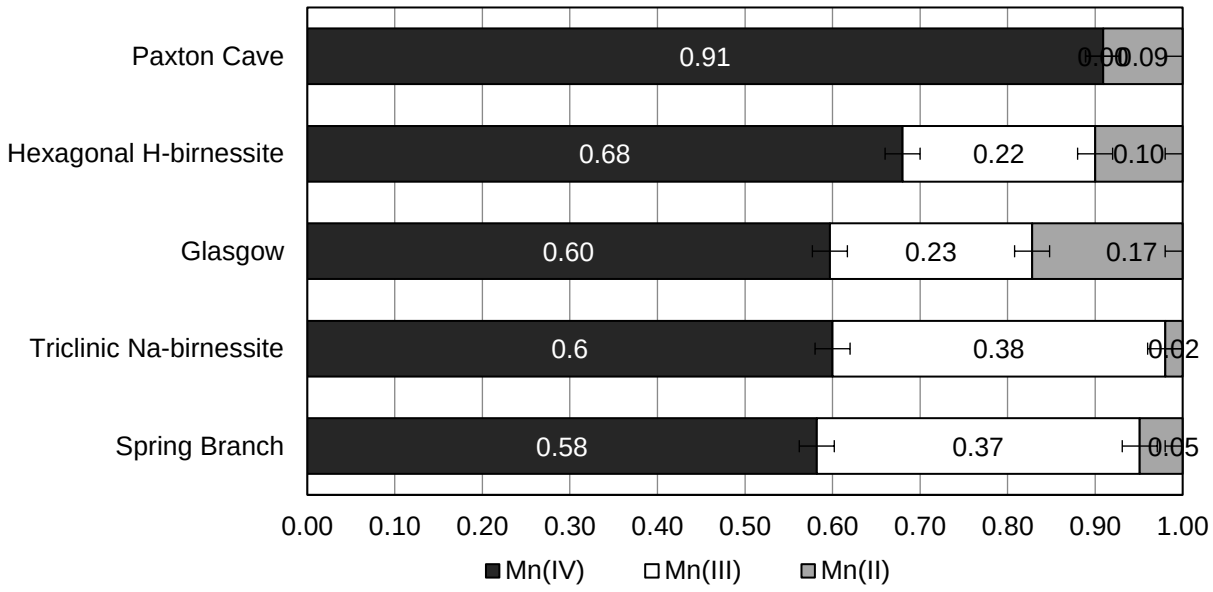

Fig. 10

This is a preprint, the final version is subject to change, of the American Mineralogist (MSA)
Cite as Authors (Year) Title. American Mineralogist, in press.
DOI: https://doi.org/10.2138/am-2020-7303

Revision 1

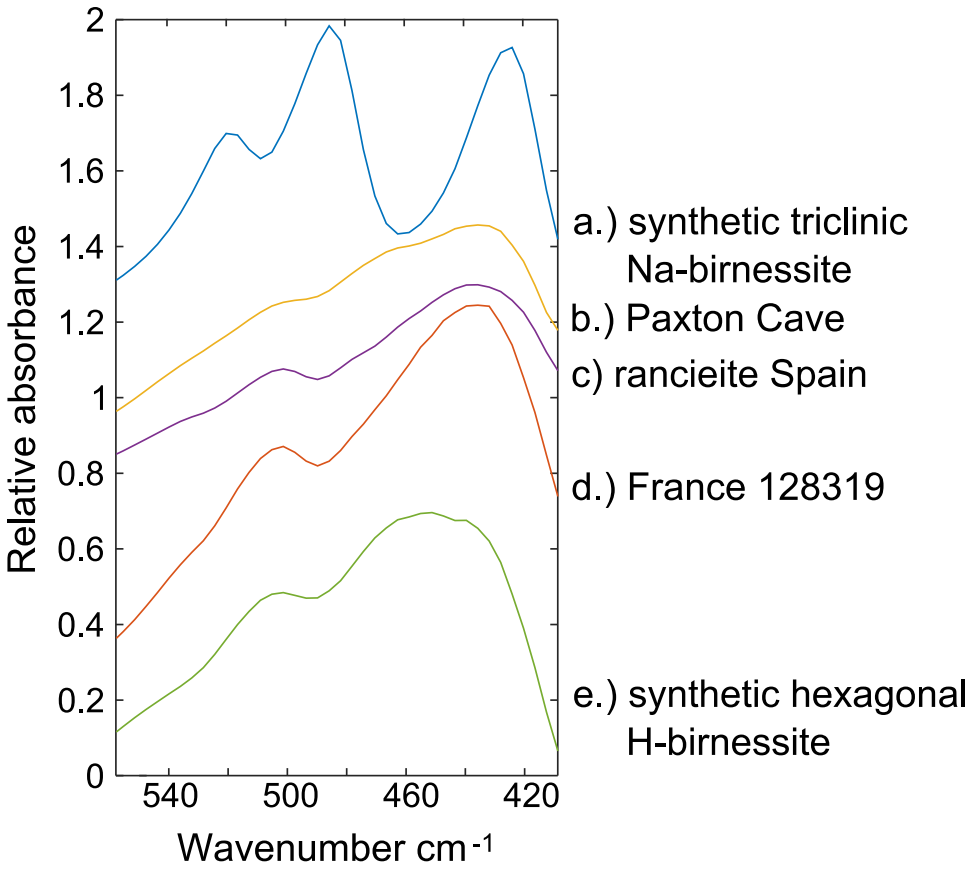

Fig. 11

This is a preprint, the final version is subject to change, of the American Mineralogist (MSA)
Cite as Authors (Year) Title. American Mineralogist, in press.
DOI: https://doi.org/10.2138/am-2020-7303

Revision 1

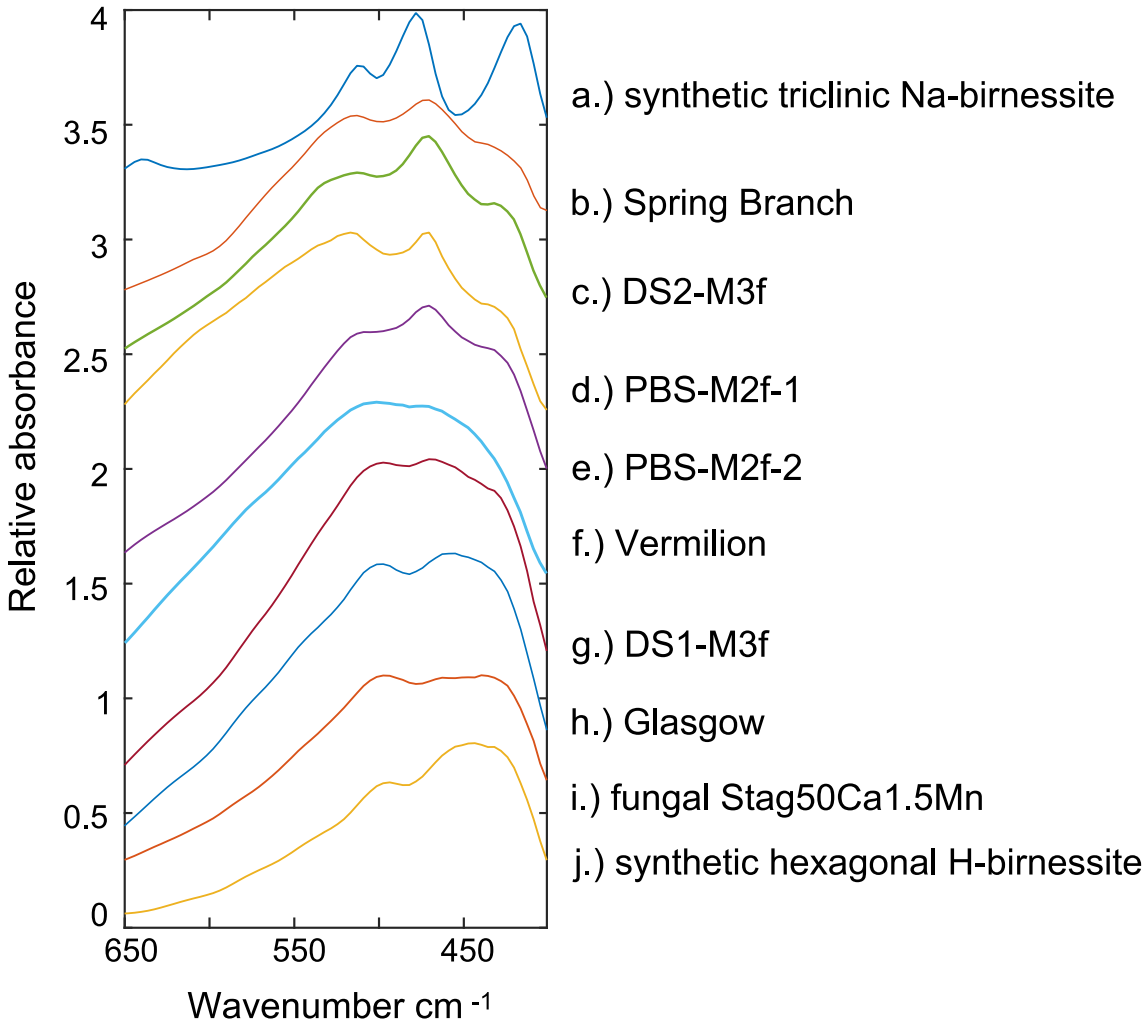

Fig. 12

This is a preprint, the final version is subject to change, of the American Mineralogist (MSA)
Cite as Authors (Year) Title. American Mineralogist, in press.
DOI: https://doi.org/10.2138/am-2020-7303

Revision 1

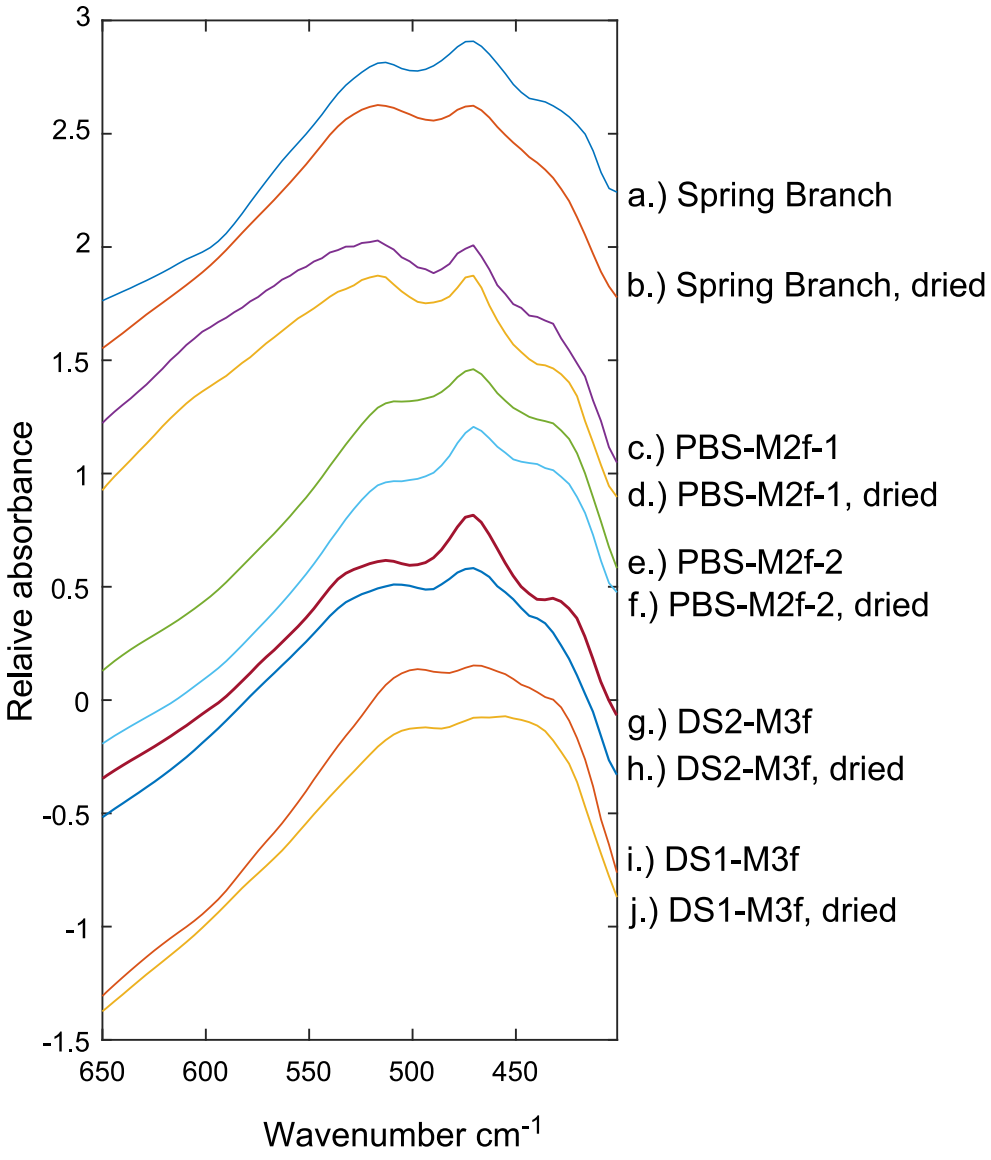

Fig. 13

This is a preprint, the final version is subject to change, of the American Mineralogist (MSA)
Cite as Authors (Year) Title. American Mineralogist, in press.
DOI: https://doi.org/10.2138/am-2020-7303

Revision 1

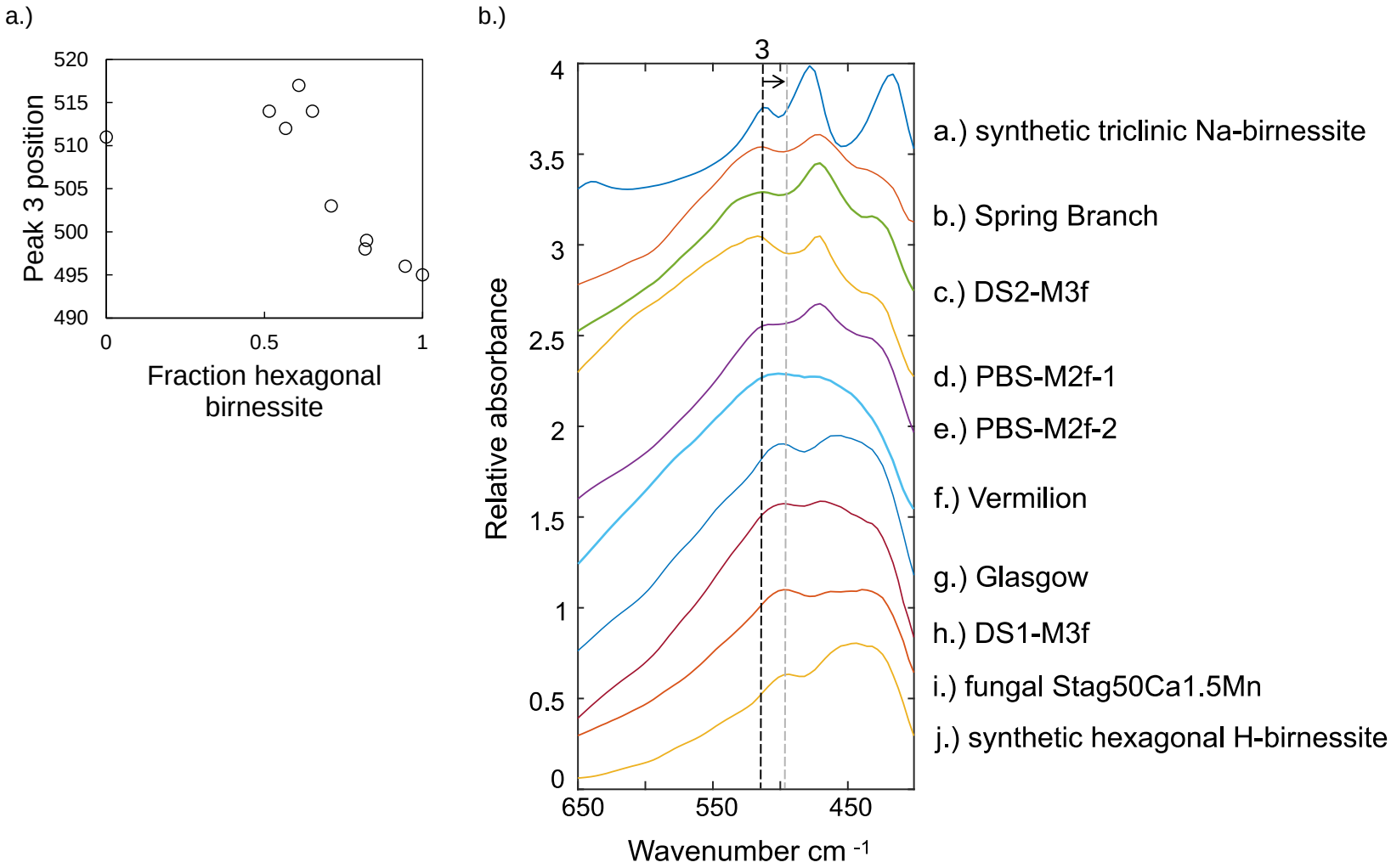

Fig. 14

This is a preprint, the final version is subject to change, of the American Mineralogist (MSA)
Cite as Authors (Year) Title. American Mineralogist, in press.
DOI: https://doi.org/10.2138/am-2020-7303

Revision 1

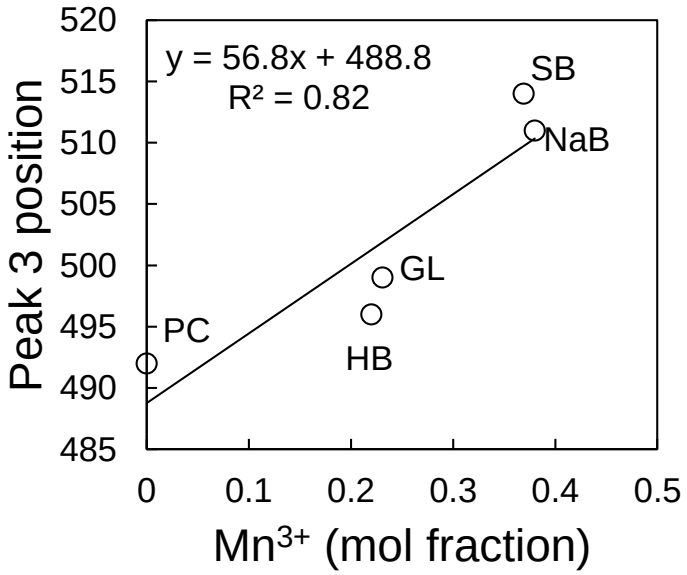

Fig. 15